Chapter 14
Stern-Gerlach Interferometry with the Atom Chip

Mark Keil, Shimon Machluf, Yair Margalit, Zhifan Zhou, Omer Amit, Or Dobkowski, Yonathan Japha, Samuel Moukouri, Daniel Rohrlich, Zina Binstock, Yaniv Bar-Haim, Menachem Givon, David Groswasser, Yigal Meir, and Ron Folman

Abstract In this invited review in honor of 100 years since the Stern-Gerlach (SG) experiments, we describe a decade of SG interferometry on the atom chip. The SG effect has been a paradigm of quantum mechanics throughout the last century, but there has been surprisingly little evidence that the original scheme, with freely propagating atoms exposed to gradients from macroscopic magnets, is a fully coherent quantum process. Specifically, no full-loop SG interferometer (SGI) has been realized with the scheme as envisioned decades ago. Furthermore, several theoretical studies have explained why it is a formidable challenge. Here we provide a review of our SG experiments over the last decade. We describe several novel configurations such as that giving rise to the first SG spatial interference fringes, and the first full-loop SGI realization. These devices are based on highly accurate magnetic fields, originating from an atom chip, that ensure coherent operation within strict constraints described by previous theoretical analyses. Achieving this high level of control over magnetic gradients is expected to facilitate technological applications such as probing of surfaces and currents, as well as metrology. Fundamental applications include the probing of the foundations of quantum theory, gravity, and the interface of quantum mechanics and gravity. We end with an outlook describing possible future experiments.

M. Keil · S. Machluf · Y. Margalit · Z. Zhou · O. Amit · O. Dobkowski · Y. Japha · S. Moukouri · D. Rohrlich · Z. Binstock · Y. Bar-Haim · M. Givon · D. Groswasser · Y. Meir · R. Folman (✉)
Department of Physics, Ben-Gurion University of the Negev, Be'er Sheva 84105, Israel
e-mail: folman@bgu.ac.il

M. Keil
e-mail: mhkeil@gmail.com

S. Machluf
Analytics Lab, Amsterdam, The Netherlands

Y. Margalit
Research Laboratory of Electronics, MIT-Harvard Center for Ultracold Atoms, Department of Physics, Massachusetts Institute of Technology, Cambridge, MA 02139, USA

Z. Zhou
Joint Quantum Institute, National Institute of Standards and Technology and the University of Maryland, College Park, Maryland 20742, USA

1 Introduction

This review follows the centennial conference held in Frankfurt in the same building housing the original Stern-Gerlach (SG) experiments. Here we describe the SG interferometry performed in our laboratories at Ben-Gurion University of the Negev (BGU) over the last decade.

The trail-blazing experiments of Otto Stern and Walther Gerlach one hundred years ago [1–4] required a few basic ingredients: a source of isolated atoms with well-specified momentum components (provided by their atomic beam), an inhomogeneous magnetic field and, if we follow the historical account of events in [5], also a smoky cigar. In this review, we present our approach to these first two ingredients, with our sincere apologies that we will not be able to adequately address the third.

As Dudley Herschbach notes [4], the SG experiments formed the basis for a "symbiotic entwining of molecular beams with quantum theory" and, as shown in many of the papers at this centennial conference, this symbiotic relationship remains vigorous to the present day. In this review, our source of isolated atoms is instead provided by the new world of ultra-cold atomic physics, to which we couple inhomogeneous magnetic fields that are provided naturally by an atom chip [6]. Current-carrying wires on such chips were first realized as magnetic traps for ultra-cold atoms at the turn of the (twenty-first) century [7–9] and reviewed extensively since [6, 10–14]. We are using the atom chip as our basis for coherently manipulating atoms in a way that is complementary to the atomic and molecular beam techniques pioneered by Otto Stern and practiced so energetically and creatively by his scientific descendants.

The work presented here is performed with high-quality atom chips fabricated by our nano-fabrication facility [15]. The atom chip is advantageous for Stern-Gerlach interferometry (SGI) for 4 main reasons. First, the source (Bose-Einstein condensates, BEC) is a minimal-uncertainty wavepacket so it is very well defined in position and momentum. Second, the source of the magnetic gradients (current-carrying wires on the atom chip) is very well aligned relative to the atomic source. Third, due to the very small atom-chip distance, the gradients are very strong, and significant Stern-Gerlach splitting can be realized in very short times. Fourth, the gradients are very well defined in time since there are no coils and the inductance of the chip wires is negligible. We will describe how these advantages have overcome long-standing difficulties and have enabled different SG configurations to be realized at BGU (e.g., spatial interference patterns [16, 17] and a "full-loop" SGI [18, 19]) alongside several applications, such as spatially splitting a clock [20, 21]. Finally, let us mention that while the interferometers presented here are of a new type, it is worthwhile noting decades of progress in matter-wave interferometry [22].

The discovery of the Stern-Gerlach (SG) effect [1] was followed by ideas concerning a full-loop SGI that would consist of freely propagating atoms exposed to magnetic gradients from macroscopic magnets. However, starting with Heisenberg [23], Bohm [24] and Wigner [25] considered a coherent SGI impractical because it was thought that the macroscopic device could not be made accurate enough to ensure a reversible splitting process [26]. Bohm, for example, noted that the magnet would

need to have "fantastic" accuracy [24]. Englert, Schwinger and Scully analyzed the problem in more detail and coined it the Humpty-Dumpty[1] (HD) effect [28–31]. They too concluded that for significant coherence to be observed, exceptional accuracy in controlling magnetic fields would be required. Indeed, while atom interferometers based on light beam-splitters enjoy the quantum accuracy of the photon momentum transfer, the SGI magnets not only have no such quantum discreteness, but they also suffer from inherent lack of flatness due to Maxwell's equations [32]. Later work added the effect of dissipation and suggested that only low-temperature magnetic field sources would enable an operational SGI [33]. Claims have even been made that no coherent splitting is possible at all [34].

Undeterred, we utilize the novel capabilities of the atom chip to address these significant hurdles. Let us briefly preview our most recent and most challenging realization, the full-loop SGI, in which magnetic field gradients act on the atom during its flight through the interferometer, first splitting, and then re-combining, the atomic wavepacket. We obtain a high full-loop SGI visibility of 95% with a spin interference signal [18, 19] by utilizing the highly accurate magnetic fields of an atom chip [6]. Notwithstanding the impressive endeavors of [35–45] this is, to the best of our knowledge, the first realization of a complete SG interferometer analogous to that originally envisioned a century ago.

Achieving this high level of control over magnetic gradients may facilitate fundamental research. Stern-Gerlach interferometry with mesoscopic objects has been suggested as a compact detector for space-time metric and curvature [46], possibly enabling detection of gravitational waves. It has also been suggested as a probe for the quantum nature of gravity [47]. Such SG capabilities may also enable searches for exotic effects like the fifth force or the hypothesized self-gravitation interaction [48]. We note that the realization presented here has already enabled the construction of a unique matter-wave interferometer whose phase scales with the cube of the time the atom spends in the interferometer [19], a configuration that has been suggested as an experimental test for Einstein's equivalence principle when extended to the quantum domain [49].

High magnetic stability and accuracy may also benefit technological applications such as large-momentum-transfer beam splitting for metrology with atom interferometry [50–52], sensitive probing of electron transport, e.g., squeezed currents [53], as well as nuclear magnetic resonance and compact accelerators [54]. We note that since the SGI makes no use of light, it may serve as a high-precision surface probe at short distances for which administering light is difficult.

For the purpose of this review, it is especially important to also realize that the atom chip allows our atoms to be completely isolated from their environment. This

---

[1]Can a fragile item be taken apart and be re-assembled perfectly? … another tough problem, according to the popular English rhyme [27]
Humpty Dumpty sat on a wall,
Humpty Dumpty had a great fall.
All the king's horses
And all the king's men
Couldn't put Humpty together again.

is demonstrated, for example, by the relatively long-term maintenance of spatial coherence that can be achieved despite a temperature gradient from 300 K to 100 nK over a distance of just 5 μm [55]. Coherence of internal degrees of freedom close to the surface has also been measured to be very high [56].

This review is organized into the following sections:

Section 2. Particle Sources: a brief discussion of how the atom chip complements and extends the century-long use of atomic and molecular beams in Stern-Gerlach experiments;

Section 3. The Atom Chip Stern-Gerlach Beam Splitter: detailing relevant aspects of the atom chip and its basic operating characteristics as a platform for SGI;

Section 4. Half-Loop Stern-Gerlach Interferometer: first realization of SGI with spatial fringe patterns;

Section 5. Full-Loop Stern-Gerlach Interferometer: first realization of the four-field complete SGI with spin population fringes;

Section 6. Applications: clock interferometry and complementarity, the matter-wave geodesic rule and geometric phase, and a T^3 interferometer realizing the Kennard phase;

Section 7. Outlook: extending the atom-chip based SGI experiments to ion beams and to massive particles.

Finally, we note that the SG effect, in conjunction with the atom chip, may also be used for novel applications without the use of interferometry. For example, we have used the SG spin-momentum entanglement to realize a novel quantum work meter. In this work, done in conjunction with the group of Juan Pablo Paz, we were able to test non-equilibrium fluctuation theorems [57].

As we hope to show in this review, we believe that the atom chip provides a novel and powerful tool for SG interferometry, with much yet to learn as SG studies enter their second century. May we continue to find surprises, fundamental insights, and exciting applications.

2 Particle Sources

Molecular beam experiments exhibiting quantum interference, diffraction, and reflection have been brought very skillfully into the modern era in presentations at this Conference by Markus Arndt, Maksim Kunitski, and Wieland Schöllkopf, and as outlined in the keynote address by Peter Toennies. In particular, Stern's vision—and realization—of diffraction of atomic and molecular beams (see, for example [4]) have found their modern expression in the work of all these experts, and many others. Here we will concentrate on a complementary approach to precisely specify internal and external quantum states and how they can be used to study interference phenomena in particular.

Table 14.1 Parameters relating to diffraction experiments using He atomic beams [58, 59], Talbot-Lau interference experiments with macromolecules [60], and interference experiments using BEC's [17] as described in this review

Type	Source	Species	Temperature (K)	σ_z (μm)	σ_{v_z} (mm/s)	$k = \sigma_{p_z}/\hbar$ ($\mu\mathrm{m}^{-1}$)	$\sigma_z\sigma_{p_z}/\hbar$	Ref.
Diffraction	Beam	^{4}He	10^{-3}	20	14	0.9	18	[58]
Diffraction	Beam	^{4}He	Not given	50	43	2.6	130	[59]
T-L interference[a]	Beam	Macromolecules	Not given	0.266	0.04	16	4.3	[60]
Interference	BEC	^{87}Rb	40×10^{-9}	6	2.8	3.8	23	[17]
Particle-on-demand[b]	Ion trap	^{40}Ca$^+$	–	0.006	900	5×10^6	3×10^4	[61, 62]
First realization	Beam	Ag	1300	30	230	400	1×10^4	[1]

The temperature shown for the beam experiments corresponds to the velocity spread superimposed on the moving frame of the longitudinal most-probable velocity. The position spread σ_z for the He beams is the beam collimator width, while the velocity spread σ_{v_z} is calculated from the beam angular divergence and its most-probable longitudinal velocity [63] ($v_x = v_{\mathrm{mp}} \approx 288$ m/s for a He beam source temperature of 8 K). For the macromolecular beam, the parameters are taken from the grating period, interferometer length, and the stated longitudinal deBroglie wavelength. Corresponding parameters for the BEC are calculated using the Thomas-Fermi approximation and a temperature at which the BEC is about 90% pure. Parameters for the original Stern-Gerlach experiment are shown for comparison in the last line. All species are in their ground electronic state. The x- and z- co-ordinates refer to the horizontal and vertical directions respectively, where the beam experiments are horizontal (so z is the transverse direction) while the BEC experiments are vertical (so z is the longitudinal direction). We do not give parameters for the "beaded atom" experiments [36] since we believe that spatial interference fringes were not observed, as explained in [64]

[a] Talbot-Lau interference, as applied to matter-wave interference studies, is described in detail in [65]. The particle species in the quoted study are functionalized oligoporphyrin macromolecules with up to 2000 atoms and masses > 25000 Da [60].
[b] These parameters are for a proposal for SGI using ion beams that will be discussed in Sect. 7.1.

Let us begin by comparing experimental parameters used in the ultra-cold atomic environment in our laboratory, typically achieved with BECs of ^{87}Rb, with corresponding state-of-the-art parameters for atomic beams. Table 14.1 summarizes parameters that are most relevant for these experiments. Note that the beam experiments are conducted in a horizontal plane, transverse to the beam propagation direction, while our BEC interference experiments are conducted in an exclusively longitudinal direction with the atoms falling vertically due to gravity (and with all applied forces also acting in the longitudinal direction).

We see that ultra-cold atom localization and velocity spreads are on the same order as transverse localization from the exemplary atomic and molecular beam experiments quoted here but, of course, ultra-cold atoms are also localized in all three dimensions, whereas the beam techniques do not achieve localization along the beam propagation axis.

3 The Atom Chip Stern-Gerlach Beam Splitter

In order to apply Stern-Gerlach splitting, our ultra-cold atomic sample needs to have at least two spin states. However, our initial atomic sample is purely in the $|F, m_F\rangle = |2, 2\rangle$ state of ^{87}Rb. After preparing a BEC on the atom chip, our SG implementation therefore begins by first releasing the magnetic trap, and then applying a radio-frequency (RF) $\pi/2$ Rabi pulse to create an equal superposition of the two internal spin states $\frac{1}{\sqrt{2}}(|1\rangle + |2\rangle)$, where $|1\rangle$ and $|2\rangle$ represent the $m_F = 1$ and $m_F = 2$ Zeeman sub-levels of the $F = 2$ manifold in the ground electronic state [66]. Transitions to other m_F levels are avoided by retaining a modest homogeneous magnetic field even after trap release. A field of about 30 G is sufficient to create an effective two-level system by pushing the $m_F = 0$ sub-level about 200 kHz out of resonance with the $|2\rangle \rightarrow |1\rangle$ RF transition due to the non-linear Zeeman effect. The intensity of the RF Rabi pulses is calibrated such that a pulse duration of 20 μs corresponds to a complete population inversion between the two states, i.e., a π-pulse. This corresponds to a Rabi frequency of $\Omega_{RF} = 2\pi \cdot 25$ kHz.

We now consider the second factor crucial to the success of our SGI experiments: fast and precise magnetic fields, in both magnitude and direction, may be delivered by pulsed currents passed through micro-fabricated wires on the atom chip. Simple Biot-Savart considerations for atom chip wires, as used in our experiments, yield magnetic field gradients of about 200 G/mm at $\sim$100 μm from the chip, which is the starting distance for most of our experiments. Accurate control of this initial position, which is also crucial for the success of the experiments, is ensured by accurate control of chip wire currents and the homogeneous magnetic field referred to above. In addition, the straight atom chip wires have very low inductance, thereby enabling the generation of well-defined magnetic force pulses with currents that are typically tens of μs long. Such pulses are, in principle, able to induce momentum

changes of hundreds of $\hbar k$.[2] Our earliest implementations of these experimental characteristics [67] were improved in subsequent apparatus upgrades [64].

Since the experiments proceed after turning off the magnetic trap, the observation time is limited by the time-of-flight (TOF) of the falling atoms and the field-of-view of our absorption imaging detection system. The latter is limited to about 4 mm, corresponding to a maximum TOF of about 28 ms. The optical detection system has a spatial resolution of about 5 μm, an important consideration for measuring spatial interference patterns (Sect. 4). Further experimental details may be found in several recent Ph.D. theses from our laboratory [64, 67, 68].

The Stern-Gerlach beam splitter (SGBS), first implemented in [16], begins with an equal superposition of $|1\rangle$ and $|2\rangle$ as described above and depicted schematically in Fig. 1. We then apply a magnetic field gradient $\nabla|\mathbf{B}|$ for duration T_1, which creates a state-dependent force $\mathbf{F}_{m_F} = m_F g_F \mu_B \nabla|\mathbf{B}|$ on the atomic ensemble, where μ_B, g_F, and m_F denote the Bohr magneton, the Landé factor, and the projection of the angular momentum on the quantization axis, respectively.

The magnetic potential created by the atom chip can be approximated as a sum of a linear part with characteristic force $\mathbf{F}$ and a quadratic part with characteristic frequency ω. After this magnetic gradient splitting pulse, the new state of the atoms is given by $\psi_f = \frac{1}{\sqrt{2}}(|1, p_1\rangle + |2, p_2\rangle)$, where $\mathbf{p}_i = \mathbf{F}_i T_1$ ($i = 1, 2$). This state represents a coherent superposition of two distinct momentum states, which are then allowed to separate spatially, thereby completing the operation of momentum and spatial splitting.

As we discuss further in the following sections, the SGBS can be extended as a tool for SGI. We describe two main configurations: a "half-loop" configuration in which the separated wavepackets are allowed to propagate freely, expand and eventually overlap, producing spatial interference patterns analogous to a double-slit experiment, and a "full-loop" configuration in which the wavepackets are actively re-combined, analogous to a Mach-Zehnder interferometer.

By applying additional pulses with different timing, these methods have been used to demonstrate, to the best of our knowledge, the first Stern-Gerlach spatial fringe interferometer (Sect. 4, [16, 17]), the first full-loop Stern-Gerlach interferometer (Sect. 5, [18, 19]), and several applications that we will describe in Sect. 6, including experiments to simulate the effect of proper time on quantum clock interference [20, 21].

4 Half-Loop Stern-Gerlach Interferometer

The two separated wavepackets generated by the SGBS initiate the pulse sequence shown in Fig. 2. Just after the SG splitting pulse, another RF $\pi/2$ pulse (10 μs dura-

---

[2]We express the momentum transfer in units of $\hbar k$, a reference momentum of a photon with 1 μm wavelength, in order to compare with atom interferometry based on optical beam splitters.
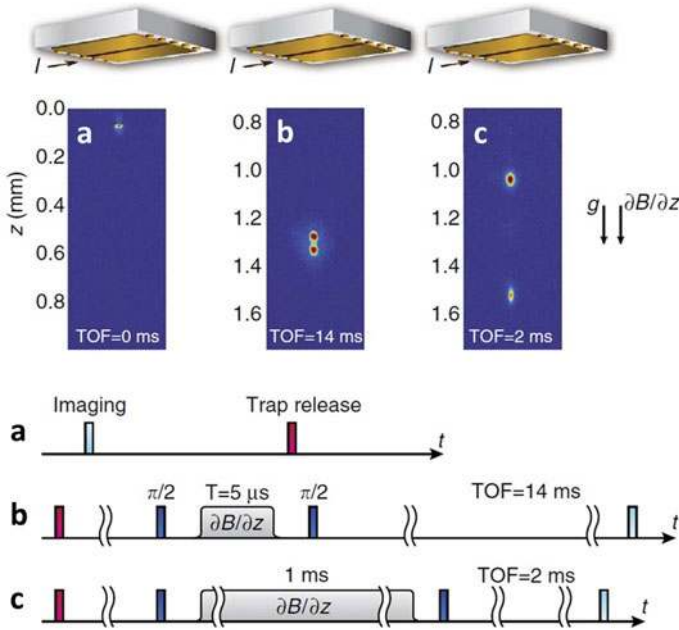
Fig. 1 The Stern-Gerlach beam-splitter (SGBS) at work [16, 67]. SGBS (a) input and (b, c) output images, and the corresponding schematic descriptions. The top row depicts our atom chip, with a pulsed current I being used to generate the magnetic gradient $\partial B/\partial z$ (we currently use three parallel wires with equal currents but opposing polarities). The chip faces downwards so that atoms can separate vertically during their free fall. (a) A magnetically trapped BEC in state $|2\rangle$ before release. (b) After a weak splitting of less than $\hbar k$ using a 5 μs magnetic gradient pulse and allowing a TOF of 14 ms. (c) After a strong splitting of more than 40 $\hbar k$ using a 1 ms magnetic gradient pulse and allowing a TOF of 2 ms. Interferometric signals are formed either as spatial interference fringes by passively allowing overlap of the wavepackets (the "half-loop" SGI), or as spin-state population oscillations upon actively recombining them (the "full-loop" SGI), as described in Sects. 4 and 5 respectively. Adapted from [16].

tion) is applied, creating a wavefunction consisting of four wavepackets [67], of which we are concerned only with the two $|2\rangle$ wavepackets having momenta $\mathbf{p}_1$ and $\mathbf{p}_2$ (the $|1\rangle$ components can be disregarded since they appear at different final positions on completing the pulse sequence and a TOF).

The time interval between the two RF pulses (in which there are only two wavepackets, each having a different spin) is reduced to a minimum ($\sim 40 \mu s$) to suppress the hindering effects of a noisy and uncontrolled magnetic environment, thereby removing the need for magnetic shielding. After a magnetic gradient pulse of duration T_2, designed to stop the relative motion of the two wavepackets, the atoms fall under gravity for a relatively long TOF, expanding freely until they overlap to create spatial interference fringes as shown schematically in Fig. 2 and experimentally in Fig. 3.
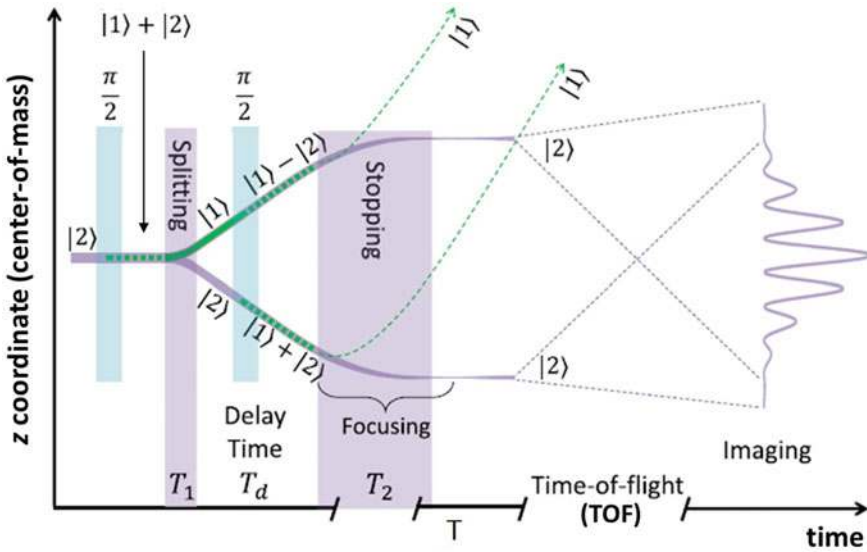
Fig. 2 Schematic depiction of the longitudinal half-loop SGI giving rise to spatial interference fringes (vertical position z in the center-of-mass frame vs. time). The initial wavepacket $|2\rangle$ (extreme left) is subjected to a $\pi/2$ pulse (blue column) that transfers the atoms into the superposition state $|1\rangle + |2\rangle$. The first magnetic gradient pulse of duration T_1 (purple column) induces a Stern-Gerlach splitting into $|1\rangle$ (green curve) and $|2\rangle$ (purple curve) having momenta $\mathbf{p}_1$ and $\mathbf{p}_2$, respectively. We then immediately apply a second $\pi/2$ pulse that places these diverging $|1\rangle$ and $|2\rangle$ states into equal superpositions $|1\rangle \mp |2\rangle$ as shown. The delay time T_d allows these wavepackets to spatially separate (in the z direction). The duration T_2 of a second gradient pulse is tuned to bring the momentum difference between the $|2\rangle$ components close to zero (see text), allowing their space-time trajectories to become parallel (solid purple curves) while expelling the $|1\rangle$ components (dotted green trajectories). The atoms then fall freely under gravity. Given sufficient time-of-flight, the two $|2\rangle$ wavepackets expand (dotted purple lines) and eventually overlap to generate spatial interference fringes, which are measured by taking an absorption image of the atoms. We note that due to the curvature of the magnetic field forming the magnetic gradient pulse, the long T_2 pulse also focuses the wavepackets, as depicted in the figure. In fact, this focusing accelerates the process of final expansion, thereby creating the two-wavepacket overlap in a shorter time. Adapted from [17] with permission © IOP Publishing & Deutsche Physikalische Gesellschaft. CC BY 3.0

The period of the interference fringes must be large enough to be observable with the spatial resolution of our imaging system (about $5\,\mu$m). This is accomplished if two conditions are fulfilled. First, the distance between the two wavepackets, d, should not be too large, since in principle the fringe periodicity varies as ht/md when the relative momentum is zero, where h, t, and m are the Planck constant, TOF duration, and the atomic mass, respectively. Second, the momentum difference between the two wavepackets should be smaller than their momentum width to avoid orthogonality. This is accomplished by tuning the duration T_2 of the second gradient pulse, which can stop the relative motion of the two $|2\rangle$ wavepackets; despite being in the same spin state, the slower wavepacket experiences a stronger impulse than
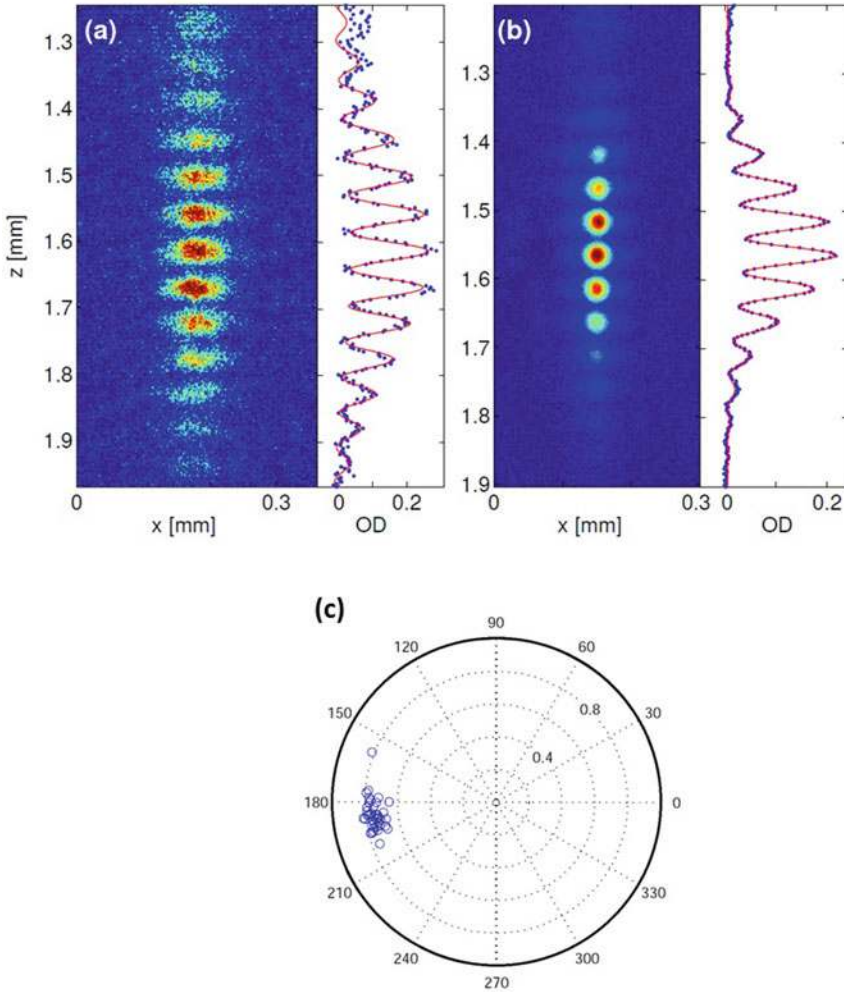
Fig. 3 Spatial interference patterns from the Stern-Gerlach interferometer. **a** A single-shot interference pattern of a thermal cloud with a negligible BEC fraction, fitted to Eq. (1) with a visibility of $V = 0.65$ (only slightly lower than single-shot visibilities typically measured for a BEC). **b** A multi-shot image made by averaging 40 consecutive interference images using a BEC (no correction or post-selection) with a normalized visibility of $V_N = 0.99$. **c** Polar plot of phase $0° \leq \phi \leq 360°$ versus visibility $0 \leq V \leq 1$ obtained from fitting each of the 40 consecutive images averaged in (**b**). The experimental parameters are $(T_1, T_d, T_2) = (4, 116, 200)\,\mu$s. Adapted from [64]

the faster one since it is considerably closer to the atom chip after the relatively long delay time T_d. We have found that zeroing the momentum difference between the two wavepackets is very robust [67].

Given that the final momentum difference between the two interfering wavepackets is smaller than their momentum spread, they overlap after a sufficiently long TOF and an interference pattern appears with the approximate form:

$$n(z, t) = A \exp \left[-\frac{(z - z_{CM})^2}{2\sigma_z(t)^2} \right]$$
$$\times \left[1 + V \cos \left(\frac{2\pi}{\lambda}(z - z_{ref}) + \phi \right) \right], \tag{1}$$

where A is the amplitude, z_{CM} is the center-of-mass (CM) position of the combined wavepacket at the time of imaging, $\sigma_z(t) \approx \hbar t / 2m\sigma_0$ is the final Gaussian width, $\lambda \approx 2\pi \hbar t / md$ is the fringe periodicity ($d = |z_1 - z_2|$ is the distance between the wavepacket centers), V is the interference fringe visibility, and $\phi = \phi_2 - \phi_1$ is the global phase difference. The vertical position z is relative to a fixed reference point z_{ref}. The phases ϕ_1 and ϕ_2 are determined by an integral over the trajectories of the two wavepacket centers. We emphasize that Eq. (1) is not a phenomenological equation, but rather an outcome of our analytical model [16].

In order to characterize the stability of the phase, which is the main figure of merit in interferometry, we average multiple experimental images with no post-selection or alignment (each single-shot image is a result of one experimental cycle). Large fluctuations in the phase and/or fringe periodicity in a set of single-shot images would result in a low multi-shot visibility, while small fluctuations correspond to high multi-shot visibility. The multi-shot visibility is therefore a measure of the stability of the phase and periodicity. Single-shot and multi-shot visibilities are all extracted by fitting to Eq. (1) after averaging the experimental images along the x direction (see Fig. 3) to reduce noise. We note that these procedures have been used over several years of half-loop SGI studies [16, 17], while the experimental results were simultaneously being greatly improved by significant modifications to the original apparatus [64, 67].

For a pure superposition state, as in our model, perfect fringe visibility V would be 1. A quantitative analysis of effects reducing V appears in [17, 64]. Some of these effects are purely technical, e.g., imperfect BEC purity and wavepacket overlap in 3D, as well as various imaging limitations etc. Such technical effects are irrelevant to the phase and periodicity stability shown by the multi-shot visibility, so we normalize the latter to the mean of the single-shot visibilities taken from the same sample: $V_N \equiv V_{avg}/\langle V_s \rangle$, where V_{avg} is the (un-normalized) visibility of the multi-shot average extracted from the fit and $\langle V_s \rangle$ is the mean visibility of the single-shot images which compose that multi-shot image. The normalized multi-shot visibility thus reflects shot-to-shot fluctuations of the global phase ϕ and the fringe periodicity λ. We note that some BEC intrinsic effects, such as phase diffusion, would not lead to a reduction of the single-shot visibility, but may cause the randomization of the shot-to-shot phase. However, such effects are expected to be quite weak, since atom-atom interactions rapidly become negligible as the BEC expands in free-fall, and the experiment may be described by single-atom physics.

Representative results from the above analysis are shown in Fig. 3. The very high (normalized) visibility shown in (b) demonstrates that the phase and periodicity are highly reproducible for each experimental cycle, the former being particularly emphasized in plot (c). High-visibility fringes ($V > 0.90$) were observed over a wide variety of experimental parameters, covering a range of maximum separations and velocities between the wavepackets. In particular, we conducted experiments at the apparatus-limited maximum value of $T_d = 600\,\mu$s (which also required a long TOF$= 21.45$ ms) in order to maximize the spatial separation of the wavepackets during their time in the interferometer. These measurements achieved a separation $d = 3.93\,\mu$m, a factor of 20 larger than the atomic wavepacket size (after focusing, see Fig. 2), while maintaining a normalized visibility of $V_N = 0.90$ [17].

Given that our observed stable interference fringes arise from such well-separated paths, these experiments demonstrate what is, to the best of our knowledge, the first implementation of spatial SG interferometry. This achievement is due to three main differences compared with previous SG schemes. Firstly, we have used minimal-uncertainty wavepackets (a BEC) rather than thermal beams. Secondly, while the splitting is based on two spin states, the wavepackets in the two interferometer arms are in the same spin state for most of the interferometric cycle, thus reducing their sensitivity to disruptive external magnetic fields. Finally, chip-scale temporal and spatial control allows the cancellation of path difference fluctuations. It should also be noted that a longitudinal SGI, based on a particle beam source, cannot take images of spatial fringes due to the high velocity of the fringe pattern in the lab frame.

This, however, is not yet the four-field SGI originally envisioned shortly after the original Stern-Gerlach experiments (as recounted in [26]), since the separated wavepackets are not actively recombined in both position and momentum. The two remaining magnetic gradients required to complete such a "closed" SGI are discussed in the following section.

5   Full-Loop Stern-Gerlach Interferometer

Clearly, if a wavepacket can be coherently reconstructed after SG splitting and recombination in a four-field configuration [26], it should be possible to observe an interference pattern at the output of such an SGI. To the best of our knowledge however, no such interference pattern has heretofore been measured experimentally, and this is the task that we now describe, many details of which are taken from [64] and references therein.

The device envisioned consists of four successive regions of magnetic gradients giving rise to the operations of splitting, stopping, reversing and, finally, stopping the two wavepackets, as shown schematically in Fig. 4a. If executed perfectly, the two wavepackets would arrive at the output of such an interferometer with a minimal relative spatial displacement and momentum difference, so that an arbitrary initial spin state should be recoverable, using the spin state of the recombined wavepacket as the interference signal. However, the operation of such an interferometer was
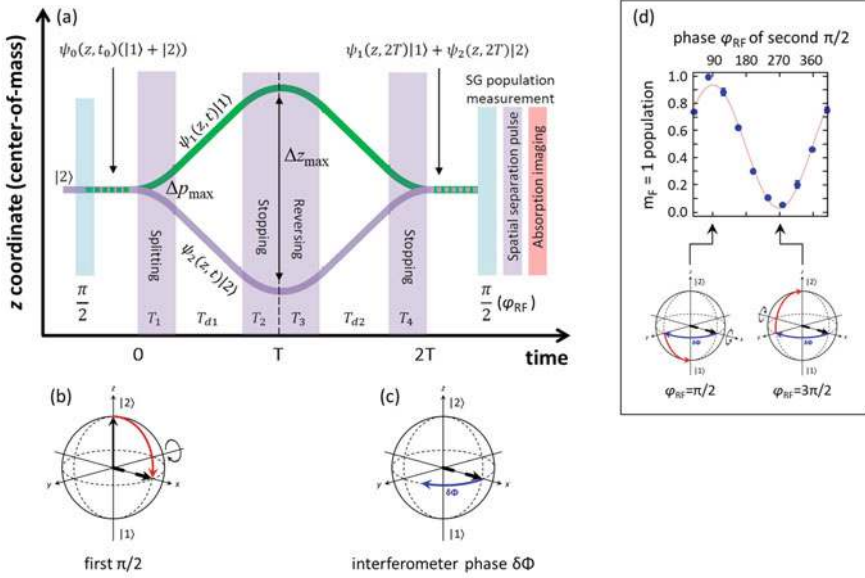
Fig. 4 The longitudinal full-loop SGI giving rise to spin population oscillations, plotted in the center-of-mass frame as in Fig. 2. **a** The sequence consists of RF pulses (blue) to manipulate the inner (spin) degrees of freedom and magnetic gradients (purple) to control the momentum and position of the wavepackets. The interferometer is prepared from the initial wavepacket $|2\rangle$ (extreme left) by applying a $\pi/2$ pulse that transfers the atoms into the superposition state $|1\rangle + |2\rangle$ [Bloch sphere shown in (**b**)]. The first magnetic gradient pulse at $t = 0$ induces a Stern-Gerlach splitting into $|1\rangle$ (green curve) and $|2\rangle$ (purple curve). Three additional magnetic gradient pulses are used to stop the relative motion of the wavepackets (at their maximum separation Δz_{max}), reverse their momenta, and finally stop them at the same position along z. The re-combined wavepacket at $t = 2T$ is therefore written as $\psi_1(z, 2T)|1\rangle + \psi_2(z, 2T)|2\rangle$, shown in (**c**) for an arbitrary interferometer phase $\delta\Phi$. After recombination, the population in $|1\rangle$ is measured by applying a second $\pi/2$ pulse with variable phase φ_{RF}, followed by a magnetic gradient to separate the populations and a subsequent pulse of the imaging laser. We expect to observe spin population fringes, i.e., oscillations in the $m_F = 1$ population, as we scan φ_{RF}, as indeed shown by the experimental results in (**d**), for which the measured visibility is 95%. The Bloch spheres in (**d**) show the particular case in which the initial vector (dashed black arrow) acquires an interferometer phase $\delta\Phi = \pi/2$ (blue arrow) followed by rotations about the $+x$ ($\varphi_{RF} = \pi/2$) or $-x$ ($\varphi_{RF} = 3\pi/2$) axes respectively (red arrows). The states $|F, m_F\rangle = |2, 2\rangle \equiv |2\rangle$ and $|2, 1\rangle \equiv |1\rangle$ are defined along the z axis in the Bloch spheres. Adapted from [64].

considered to be technically impractical, since coherent recombination of the two beam paths would require extremely precise control of the magnetic fields [24].

Our experiments begin, as before, with a $\pi/2$ pulse creating a superposition of the two spin states $|1\rangle$ and $|2\rangle$ of ^{87}Rb that is subsequently split into two momentum components by a magnetic gradient pulse (along the vertical axis z) as described in Sects. 3 and 4. Additional magnetic gradient pulses are needed to "close" the loop of such an interferometer, i.e., to overlap the wavepackets spatially and with zero relative momentum. To stop the relative motion of the two wavepackets after the

first pulse, and to accelerate them backwards, we reverse the current on the atom chip, causing the force applied by the magnetic field gradient to be in the opposite direction. Alternatively, we can apply a spin inversion procedure by using a π Rabi pulse that inverts the population between the two internal states, following which a magnetic gradient pulse will then apply the opposite differential momentum to the two wavepackets. We obtain the signal with the help of a second $\pi/2$ pulse, followed by a spin population measurement. We measure the visibility by scanning the phase φ_{RF} of this $\pi/2$ pulse.

Our full-loop interferometer is implemented with an experimental system in which care is taken to reduce a wide range of hindering effects relative to our earliest work [16]. For example, a new atom chip was installed, utilizing a 3-wire configuration to produce a quadrupole magnetic field whose zero is at the precise height of the BEC. This reduces phase fluctuations by exposing the wavepackets to a weaker magnetic field while still generating strong magnetic gradients.

The practical difficulty encountered in re-assembling the original wavefunction was named the Humpty-Dumpty (HD) effect [28–30], implying that the initial wavepacket breaks under the SG field and cannot be reunited, as noted in the brief historical perspective given in Sect. 1. Quantitatively, the spin coherence, which is measurable as the visibility V of the observed spin fringes, is expressed as [29]

$$V = \exp\left\{-\frac{1}{2}\left[\left(\frac{\Delta z(2T)}{\sigma_z}\right)^2 + \left(\frac{\Delta p_z(2T)}{\sigma_p}\right)^2\right]\right\}, \qquad (2)$$

where $\Delta z(2T)$ and $\Delta p_z(2T)$ denote the mismatch between the wavepackets in their final position and momentum respectively, after the interferometer duration $2T$ (Fig. 4a), and σ_z and σ_p are the corresponding initial wavepacket widths. Equation (2) summarizes the main result of the HD papers in relation to our experimental observable. We emphasize that this reduction in visibility has nothing to do with effects of decoherence due to some coupling with the environment. We also note that the above HD calculation is done for a minimal-uncertainty wavepacket. For the general case, one can identify $l_z = \hbar/\sigma_p$ and $l_p = \hbar/\sigma_z$ as the relevant scales for coherence [26, 29], where l_z and l_p are the spatial coherence length and the momentum coherence width, respectively.

Let us discuss the meaning of this equation. The quantities σ_z and σ_p characterize the initial atomic wavefunction, and are thus microscopic quantities. The quantities Δz and Δp_z describe the experimental imprecision in the final recombination. In a "good" SG experiment (i.e., one which allows "unmistakable" splitting [29]) the maximum values of splitting in position and momentum should be much larger than their respective initial widths, meaning they should be macroscopic. On the other hand, according to Eq. (2), a nearly perfect maintenance of spin coherence ($V \simeq 1$) requires both $\Delta z \ll \sigma_z$ and $\Delta p_z \ll \sigma_p$. Consequently, Eq. (2) tells us that we need to recombine macroscopic quantities with a microscopic level of precision. This is the challenge facing SG interferometer experiments.

It is interesting to note that in the half-loop experiments, we found that Δp_z can be quite large (rendering the trajectories during the TOF period in Fig. 2 slightly non-parallel) without significantly reducing the measured spatial interference fringe visibility, so the stability of the half-loop experiments cannot be used to examine the HD equation. This robustness of the half-loop may also be understood by considering the fact that the expansion of the wavepackets creates an enhanced local coherence length, since for every region of space the k vector variance becomes smaller as TOF increases (see also [69, 70]).

A practical full-loop SG experiment must consider and address two effects. First, as noted above, the HD effect requires accurate recombination, namely, small Δz and Δp_z. These small values must be maintained for many experimental cycles, and thus a high level of stability in these values is also important. Achieving accurate recombination means that the overlap integral, calculated in Eq. (2), will have a significant non-zero value. Second, one must maintain a stable interferometer phase $\delta\Phi$, so that it has the same value shot-to-shot. This requires that the coupling to external magnetic noise is kept to a minimum, either by shielding the experiment and stabilizing the electronics (e.g., responsible for the homogeneous magnetic fields), or by conducting the experiment extremely quickly so that such environmental fluctuations do not have time to introduce significant phase noise.

Our full-loop SGI yields a visibility up to 95% (Fig. 4d), proving that we are able to use the SG effect to build a full-loop interferometer as originally envisioned almost a century ago. We note three differences between our realization and the scheme considered in the HD papers: (1) We use a BEC, which is a minimum-uncertainty wavepacket, whereas the HD papers considered atomic beam experiments with large uncertainties on the order of $\sigma_z\sigma_p \simeq 10^3$; (2) We implement fast magnetic gradient pulses generated by running currents on the atom chip, in contrast to using constant gradients from permanent magnets that were considered in the original proposals; (3) Our interferometer is a 1D longitudinal interferometer, while the originally envisioned SGI was 2D, i.e., it enclosed an area.

The full-loop experiments include a wide variety of optimizations and checks (see [64] for additional details). To make sure the spin superposition is not dephased due to some slowly varying gradients in our bias fields, we add π pulses giving rise to an echo sequence. To access a larger region of parameter space and to ensure the robustness of our results, we use several different configurations by, for example, implementing the reversing pulse (T_3) by inverting the sign of the atom chip currents vs. inverting the spins with the help of π pulses. We also utilize a variety of magnetic gradient magnitudes, and scan both the splitting gradient pulse duration T_1 and the delay time between the pulses T_d. All results are qualitatively the same. For weak splitting we observe high visibility ($\sim$95%), while for a momentum splitting equivalent to $\hbar k$ the visibility is still high ($\sim$75%), indicating that the magnet precision enabled coherent spin-state recombination to a high degree.

Finally, we briefly compare our experiments to previous work in an elaborate series of SGI experiments over a period of 15 years using metastable atomic beams [35–42, 44] and, more recently, thermal and ultra-cold alkali atoms [43, 45]. A detailed discussion is given in [64]. While these longitudinal beam experiments did observe

spin-population interference fringes, the experiments reviewed here are very different. Most importantly, an analogue of the full-loop configuration was never realized, as only splitting and stopping operations were applied (i.e., there was no recombination) and wavepackets emerged from the interferometer with the same separation as the maximal separation achieved within (see Fig. 2 of [40] and Footnote [10] of [43]). We have not found anywhere in the many papers published by this group (only some of which are referenced here) evidence of four operations being applied as required for a full-loop configuration, whether the experiment was with longitudinal or transverse gradients. In addition, no spatial interference fringes were observed, as the spatial modulation they observed was a signature of multiple parallel longitudinal interferometers, each having its own individual relative phase between its two wavepackets.

To conclude, we have shown that a full-loop has been realized [18, 121]. In addition, as previously shown in Heisenberg's argument, the momentum splitting is the figure of merit in determining the phase dispersion. In our experiment, coherence is observed up to a momentum splitting as high as $\Delta p_z(T_1)/\sigma_p = 60$. However, in contrast, the visibility is more sensitive to spatial splitting and we achieve $\Delta z(T)/\sigma_z = 4$, much lower than for the half-loop, where we achieved $\Delta z/\sigma_z = 18$. The splitting is coherent but its, limits in terms of the HD effect are yet to be explored quantitatively. Many mysteries remain to be solved, such as why is the observed reduction not symmetric in momentum and spatial splitting, in contrast to Eq. 2. A simple answer, which is yet to be examined in detail, is the existence of some sort of spatial decoherence mechanism due to the environment.

Having now described the SG beam-splitter, the SG half-loop, and the SG full-loop, we show in the next section how these techniques may be used for different applications.

6 Applications

The pulse sequence in the half-loop experiments creates two spatially separated wavepackets in the state $|2\rangle$ with zero relative momentum (left-most frame of Fig. 5a–c). We now take advantage of the long free-fall period in the experiment (labelled TOF in Fig. 2, i.e., after the "stopping pulse") to further manipulate these wavepackets while they are allowed to expand and ultimately to overlap. The experiments are based on imposing a differential time evolution between the two wavepackets, which we measure as the interference patterns generated upon their recombination.

In particular, we create a "clock" state for each of the two wavepackets by first applying an RF pulse that prepares the atoms in a superposition of two Zeeman sublevels $|1\rangle$ and $|2\rangle$ whose coefficients depend on the Bloch sphere angles θ and ϕ. This superposition state is a two-level system evolving with a known period, as in the regular notion of an atomic clock. The RF pulse (duration T_R) controls the value of $C = \sin \theta$, while a subsequent magnetic gradient pulse (duration T_G) controls the value of $D_I = \sin(\phi/2)$ by changing the relative "tick" rate $\Delta \omega$ of the two

clock wavepackets, as illustrated in Fig. 5a–c. The quantities C and D_I describe
the clock preparation quality and the ideal distinguishability between the two clock
interferometer arms respectively, which we will find quantitatively useful in our
discussion of clock complementarity [see Eqs. (4) and (5)]. We note that, although
the magnetic gradient pulse applies a different SG force to each of the states within
the clock, we have evaluated this effect for our experimental parameters and find
that it is smaller than our experimental error bars ($\leq 2\%$, Supplementary Materials
of [21]).

6.1 Clock Interferometry

Let us first discuss the motivation for clock interferometry [20]. Time in standard
quantum mechanics (QM) is a global parameter, which cannot differ between paths.
Hence, in standard interferometry [71], a height difference in a gravitational field
between two paths would merely affect the relative phase of the clocks, shifting
the interference pattern without degrading its visibility. In contrast, general relativ-
ity (GR) predicts that a clock must "tick" slower along the lower path; thus if the paths
of a clock passing through an interferometer have different heights, a time differential
between the paths will yield "which path" information and degrade the visibility of
the interference pattern according to the quantum complementarity relation between
the interferometric visibility and the distinguishability of the wavepackets [72]. Con-
sequently, whereas standard interferometry may probe GR [73–75], clock interfer-
ometry probes the interplay of GR and QM. For example, loss of visibility because
of a proper time lag would be evidence that gravitational effects contribute to deco-
herence and the emergence of a classical world [76].

Here we describe the use of this new tool—the clock interferometer—for its poten-
tial to investigate the role of time at the interface of QM and GR. Since the genuine GR
proper time difference is too small to be measured with existing experimental tech-
nology, our experiments instead simulate the proper time difference between the
clock wavepackets using magnetic gradients, thereby causing the clock wavepackets
to "tick" at different rates. Our results in this proof-of-principle experiment show
that the visibility does indeed oscillate as a function of the simulated proper time lag.

In the ultimate experiment, each part of the spatial superposition of a clock, located
at different heights above Earth, would "tick" at different rates due to gravitational
time dilation (so-called "red-shift"). We can easily calculate the proper time differ-
ence between two arms of the clock interferometer as a figure-of-merit for this effect.
Using a first-order approximation of gravitational time dilation, and assuming a large
separation between the arms of $\Delta h = 1\,\text{m}$, an interferometer duration of $T = 1\,\text{s}$
yields a proper time difference between the arms of only $\Delta\tau \simeq Tg\Delta h/c^2 \simeq 10^{-16}\,\text{s}$.
Such a small time difference means that a very accurate and fast-ticking clock must
be sent through an interferometer with a large space-time area in order to observe the
actual GR effect. Both requirements are beyond our current experimental capabili-
ties. Our "synthetic" red-shift is created by applying an additional magnetic gradient
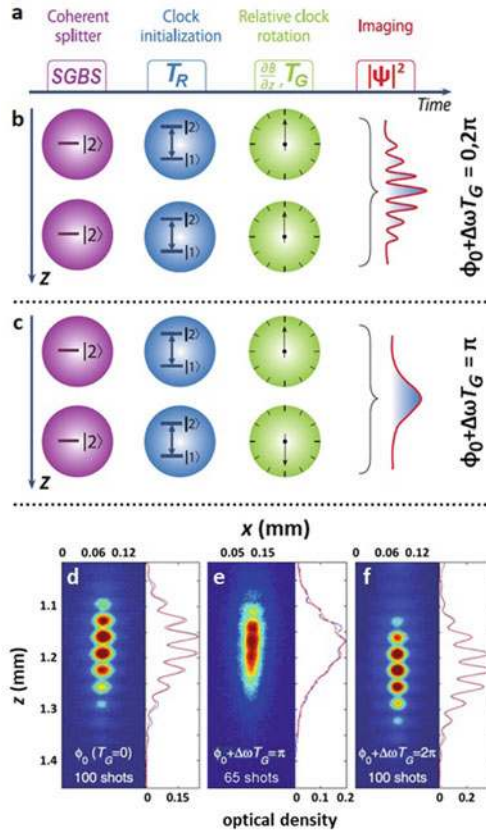
Fig. 5 Clock interferometry. **a** Timing sequence (not to scale): Following a coherent spatial splitting by the SGBS and a stopping pulse, the system consists of two wavepackets in the $|2\rangle$ state (separated along the z axis) with zero relative velocity, as in Sect. 4. The clock is then initialized with an RF pulse of duration T_R (usually a $\pi/2$ pulse, $T_R = 10\,\mu s$) after which the relative "tick" rate $\Delta\omega$ of the two clock wavepackets may be changed by applying a magnetic field gradient $\partial B/\partial z$ of duration T_G. Clock initialization occurs 1.5 ms after trap release, the first 0.9 ms of which is used for preparing the two wavepackets. The wavepackets are then allowed to expand and overlap and an image is taken. **b** Evolution in time, synchronized with (**a**). Each ball represents a clock wavepacket, where the hand represents its Bloch sphere phase ϕ_{BS}. When the clock reading (i.e., the position of the clock hand) in the two clock wavepackets is the same ($\phi_{BS} = \phi_0 + \Delta\omega T_G = 0, 2\pi$), fringe visibility is high. **c** When the clock reading is opposite (orthogonal, $\phi_{BS} = \phi_0 + \Delta\omega T_G = \pi$), there is no interference pattern. (d)-(f) Corresponding interference data of the two wavepackets, i.e., of the clock interfering with itself. All data samples are from consecutive measurements without any post-selection or post-correction. Single-shot patterns for $\phi_{BS} = \phi_0 + \Delta\omega T_G = \pi$ also show very low fringe visibility (see Fig. 2c of [20]). Adapted from [20] and reprinted with permission from AAAS; **e** is adapted from [64]

(of duration T_G) that causes the clock wavepackets to "tick" at different rates. We denote the "tick" rate difference by $\Delta\omega$.

Our results, some of which are presented in Fig. 5d–f, with more details in [20, 64], show that the relative rotation between the two clock wavepackets affects the interferometric visibility. In the most extreme case, when the two clock states are orthogonal, e.g., one in the state $\frac{1}{\sqrt{2}}(|1\rangle + |2\rangle)$ and the other in the state $\frac{1}{\sqrt{2}}(|1\rangle - |2\rangle)$, the visibility of the clock self-interference drops to near zero (Fig. 5e). By varying the duration of the magnetic gradient T_G and thereby scanning the differential rotation angle ϕ_{BS} between the two clock wavepackets, we show quantitatively that the visibility oscillates as a function of our "synthetic" red-shift with a period of $\Delta\omega T_G = 2\pi$ (Fig. 5d,f). As an additional test of the clock interferometer, we modulate its preparation by changing the duration of the clock initialization pulse T_R, which influences the relative populations of the two states composing the clock. This changes the state of the system from a no-clock state to a full-clock state in a continuous manner. The results show that the visibility behaves as expected in each case, further validating that it is the clock reading which is responsible for the oscillations in visibility that we observe as a function of T_R [20].

6.2   Clock Complementarity

These measurements of visibility may naturally be extended to study quantum complementarity for our self-interfering atomic clocks, which we again remark is at the interface of QM and GR. Our central consideration here is the inequality [77]

$$V^2 + D^2 \leq 1, \tag{3}$$

where V is the "visibility" of an interference pattern such as discussed throughout this review, and D is the "distinguishability" of the two paths of the interfering particle. The latter quantity can also be measured directly in the clock experiments by controlling the angle ϕ_{BS}, where ($\theta = \pi/2, \phi_{BS} = \Delta\omega T_G = \pi$) prepares two perfectly distinguishable clocks such that $D = 1$ (Fig. 5e). A brief account of recent work theoretically and experimentally verifying this fundamental inequality is given by [21] and references therein.

It is important to investigate clock complementarity, particularly in view of recent theoretical work showing that spatial interferometers can be sensitive to a proper time lag between the paths [78] and speculation (see Table 1 in [72]) that the inequality of Eq. (3) may be broken such that $V^2 + D^2 > 1$ when the effect of gravity is dominant. Zhou et al. summarize the importance of this work as follows: "… on the one hand, if the 'ticking' rate of the clock depends on its path, then clock time provides which-path information and Eq. (3), developed in the framework of non-relativistic QM, must apply. Yet, on the other hand, gravitational time lags do not arise in non-relativistic QM, which is not covariant and therefore not consistent with

the equivalence principle [79]. Hence our treatment of the clock superposition is a semiclassical extension of quantum mechanics to include gravitational red-shifts."

The experiments we conducted in [21] set out to test Eq. (3) quantitatively. Imperfect clock preparation (i.e., with $\theta \neq \pi/2$) reduces the measurable distinguishability D from its ideal value D_I as

$$D^2 = (C \cdot D_I)^2, \quad \text{where } C \equiv \sin\theta = 2\sqrt{P(1-P)} \tag{4}$$

and

$$D_I = |\sin(\Delta\phi/2)| \tag{5}$$

with P and $1 - P$ denoting the populations (occupation probabilities) of the two energy eigenstates of the clock and $\Delta\phi_{\text{BS}} \equiv \phi_{\text{BS}}^u - \phi_{\text{BS}}^d$, where u and d denote the upper and lower paths of the interferometer, respectively.

The experiment now has the task of measuring the three quantities V, D_I and C independently. We use the normalized visibility V_N as discussed in Sect. 4. We evaluate D_I independently by measuring the relative phases in two single-state interferometers, one for each of the two clock states, and we measure C, also independently, in a separate experiment by measuring P after the clock is initialized. Our results for these independently-measured quantities are shown in Fig. 6a, c, and e, where the results in (c) and (e) are based on analyzing the data in (b) and (d) respectively. We then combine these three quantities in the complementarity expression

$$(V_N)^2 + (C \cdot D_I)^2 \leq 1, \tag{6}$$

whereupon we see from Fig. 6f–g that the complementarity inequality [Eq. (3)] is indeed upheld for the clock wavepackets superposed on two paths through our SG interferometer.

While the relation in Eq. (6) is specific to clock complementarity, it is unusual in linking non-relativistic quantum mechanics with general relativity. A direct test of this complementarity relation will come when D_I reflects the gravitational red-shift between two paths which traverse different heights.

6.3 Geometric Phase

The geometric phase due to the evolution of the Hamiltonian is a central concept in quantum physics. In noncyclic evolutions, a proposition relates the geometric phase to the area bounded by the phase-space trajectory and the shortest geodesic connecting its end points [80–82]. The experimental demonstration of this geodesic rule proposition in different systems is of great interest, especially due to its potential use in quantum technology. Here, we report a novel experimental confirmation
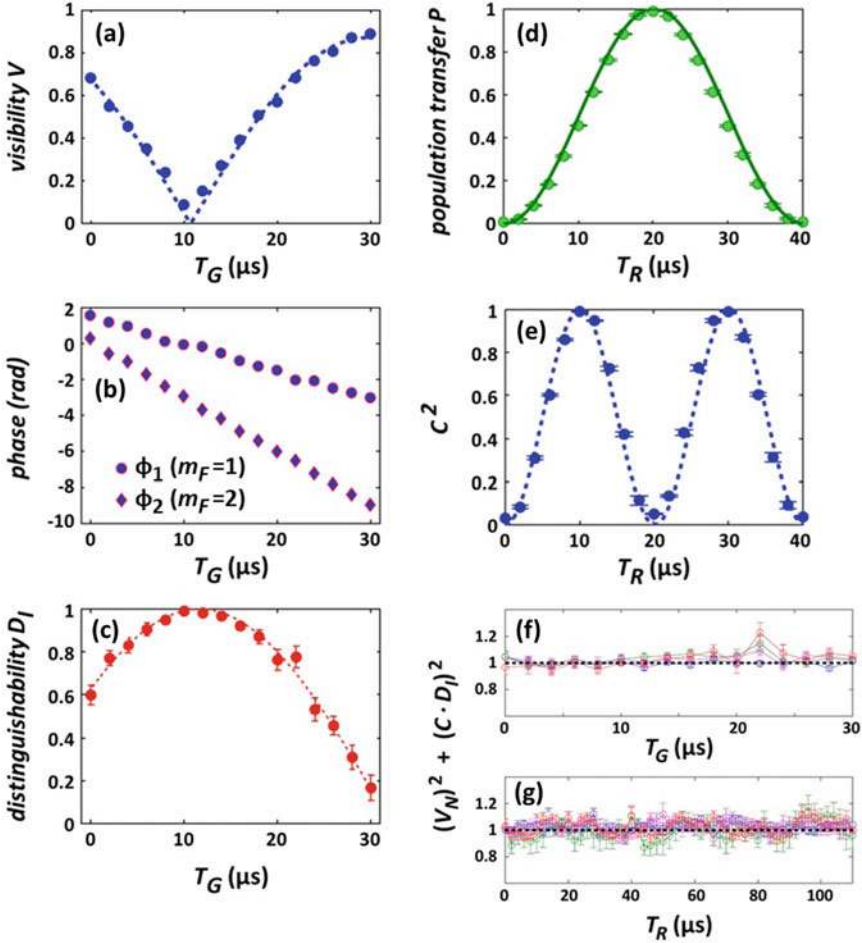
Fig. 6 Clock complementarity: **a–e** V, D_I, and C measured independently and **f–g** combined in the complementarity relations of Eqs. (3)-(6). **a** The visibility of an ideal clock ($C = 1$) interference pattern vs. T_G, fitted to $|\cos(\phi/2)|$; **b–c** the distinguishability is calculated from Eq. (5) using the difference in relative angles $\phi_2 - \phi_1$, each measured separately and shown in (**b**); and **d–e** the clock preparation quality C is calculated from Eq. (4) using the data in (**d**). Finally, **f** shows the combination of all three parameters $(V_N)^2 + (C \cdot D_I)^2$ for four values of C when D_I is scanned and **g** shows the same combination for four values of D_I when C is scanned. Only the data point in (**f**) for T_G near 22 μs differs from unity, due to a relatively large experimental error in measuring the interferometric phase. These data therefore verify clock complementarity. Adapted from [21] with permission © IOP Publishing & Deutsche Physikalische Gesellschaft, all rights reserved

of the geodesic rule for a noncyclic geometric phase by means of a spatial SU(2) matter-wave interferometer, demonstrating, with high precision, the predicted phase sign change and π jumps. We show the connection between our results and the Pancharatnam phase [83].

In the clock complementarity application just described, we scanned the third RF pulse (duration T_R) to vary the clock preparation parameter $C = \sin\theta$. In our case, a $\pi/2$ pulse typically corresponds to $T_R = 10\,\mu s$, so $T_R < 10\,\mu s$ places the Bloch vector in the northern hemisphere of the Bloch sphere with $P_1 < P_2$, while $10 < T_R < 30\,\mu s$ places the Bloch vector in the southern hemisphere ($P_1 > P_2$), i.e., the selected hemisphere is a periodic function of T_R such that an unequal superposition of $|1\rangle$ and $|2\rangle$ is created for each of the wavepackets unless θ lies on the equator. After applying this RF pulse (with some chosen duration T_R), we adjust the phase difference between the two superpositions by applying the third magnetic gradient pulse of duration T_G. This rotates the Bloch vectors along the latitude that was selected by the RF pulse to points A and B in the northern hemisphere (or A', B' in the southern hemisphere) as shown in Fig. 7a, thereby affecting the phase difference $\Delta\phi_{BS}$, which we simply call $\Delta\phi$ hereafter.

The two wavepackets are allowed to interfere as in our half-loop experiments, enabling a direct measurement of the geometric phase. As usual, we extract the "total" interference phase (labeled Φ) by fitting the fringe patterns using Eq. (1). For general values of θ and $\Delta\phi$ (i.e., after the application of both T_R and T_G), we write the total phase between the two wavepackets as [84]

$$\Phi = \arctan\left\{ \frac{\sin^2(\theta/2)\,\sin(\Delta\phi)}{\cos^2(\theta/2) + \sin^2(\theta/2)\,\cos(\Delta\phi)} \right\}. \tag{7}$$

Measurements of Φ, combined with values of θ deduced independently from the relative populations of states $|1\rangle$ and $|2\rangle$, then allow us to fit $\Delta\phi$ to high precision as a function of T_G. These measurements verified that $\Delta\phi$ depends linearly on T_G, and we found that $\Delta\phi = \pi$ occurs at $T_G = 17\,\mu s$.

Figure 7b–c shows interference fringe images for this specific value of T_G, from which we extract the total phase as shown in Fig. 7e. We see immediately that this phase is independent of θ within each hemisphere, an observation we call "phase rigidity". Moreover, the (constant) phase in each hemisphere differs by π, which can also be deduced from the vanishing visibility shown in Fig. 7d in which we have combined the data from both hemispheres. Evidently, there is a sharp jump in the phase of the interference pattern as θ crosses the equator, as suggested by the singularities in Eq. (7) that arise when $\theta = \pi(n + 1/2)$ (integer n) and $\Delta\phi = \pi$.

To understand the non-cyclic geometric phase, we need to further examine the Bloch sphere. We see that the path from $A \to B$ along the latitude θ and returning along the geodesic (or "great-circle route") from $B \to A$ encloses an area [blue shading in Fig. 7(a)] in a counter-clockwise direction, whereas the corresponding path from $A' \to B'$ and back again in the southern hemisphere proceeds in a clockwise direction. One-half of this area is the "geometric phase" that we now wish to calculate.
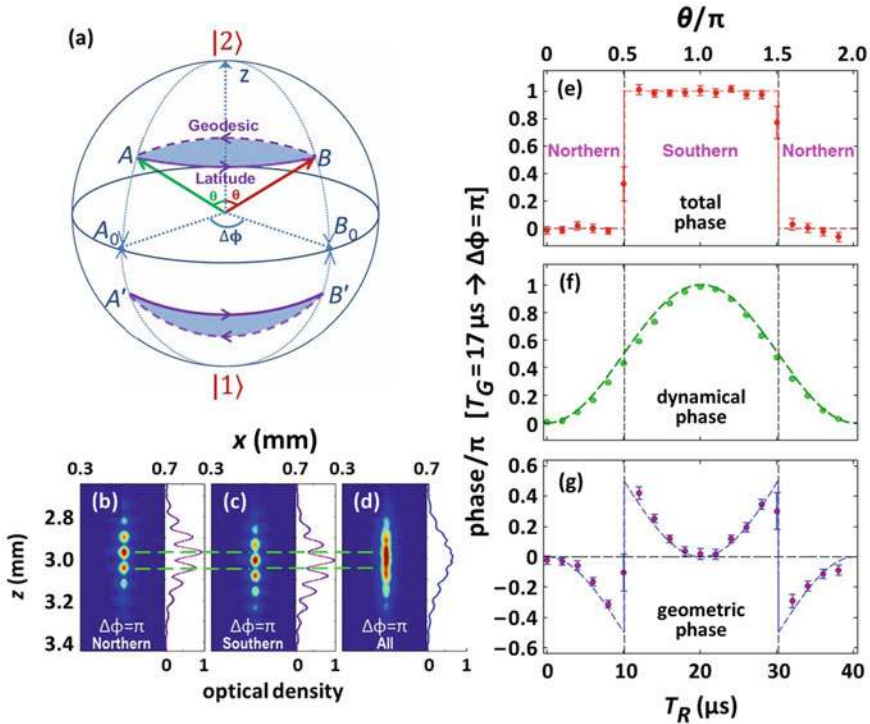
Fig. 7 Geometric phase. **a** Bloch sphere for the two wavepackets (green and red arrows labeled A and B, respectively) prepared by an RF pulse (duration T_R, rotation angle θ) and a subsequent magnetic gradient pulse (duration T_G) that induces a rotation angle difference of $\Delta\phi$. The rotation $A \rightarrow B$ lies along a constant latitude (solid purple line), while the returning geodesic $B \rightarrow A$ lies along the "great circle" curve (dashed purple line). Bloch vectors for corresponding wavepackets prepared in the southern hemisphere are shown as A' and B'. **b–c** Interference fringes generated by the half-loop SGI, averaged over a total of 330 experimental shots with varying $0 < T_R < 40\,\mu s$, while keeping a fixed value of $T_G = 17\,\mu s$ (this value of T_G corresponds to $\Delta\phi = \pi$, see text). The dashed green lines show that the maxima in (**b**) lie exactly where the minima occur in (**c**), corresponding to Bloch vectors prepared in the northern and southern hemispheres, respectively. Adding all these interference patterns together in (d) shows near-zero visibility, i.e., they are completely out of phase. The fact that exactly the same pattern is observed while in the same hemisphere, independent of θ (duration of T_R), is called "phase rigidity". **e** Total phase extracted from the interference fringes measured as a function of the RF pulse duration (lower scale) and the corresponding latitude θ (upper scale). Phase rigidity is clearly visible. **f–g** Dynamical and geometric phases extracted from the data in (**e**) and independently measured values of θ and $\Delta\phi$ (see text). The range of T_R in (**e–g**) (T_G is fixed at $17\,\mu s$) corresponds to a full cycle from the northern hemisphere ($0 < T_R < 10\,\mu s$) through the southern hemisphere ($10 < T_R < 30\,\mu s$), and back to the north pole at $T_R = 40\,\mu s$. Adapted from [84] with permission © the authors, some rights reserved; exclusive licensee AAAS.

The total phase change Φ for closed paths like $A \to B \to A$ and $A' \to B' \to A'$ is a sum of two contributions, the dynamical phase Φ_D and the geometric phase Φ_G. The dynamical phase is given by [80]

$$\Phi_D = \frac{\Delta\phi}{2}\left(1 - \cos\theta\right), \tag{8}$$

which can be determined by measuring θ and $\Delta\phi$ independently. For the particular value of $\Delta\phi = \pi$ chosen as a sub-set of our experimental data, we are then able to present Φ_D in Fig. 7f. Finally, we subtract the phases Φ_D, as plotted in (f), from the total phases Φ plotted in (e) (which, as noted above, are extracted directly from the observed interference pattern) to obtain the phases Φ_G. Namely, we perform $\Phi - \Phi_D$ and get Φ_G, which is presented in Fig. 7g. Let us emphasize that the total phase Φ is also the Pancharatnam phase [83], and thus our experiment is also a direct measurement of this phase.

Our plot of Φ_G exactly confirms the prediction shown in Fig. 4d of [81], also reproduced as the dashed blue line in Fig. 7g. The predicted sign change as the latitude crosses the equator is clearly visible. The evident phase jump is due to the geodesic rule. When $\Delta\phi = \pi$, the geodesic must go through the Bloch sphere pole for any $\theta \neq \pi/2$. As the latitude approaches the equator (i.e., increasing θ), the blue area in Fig. 7a (twice Φ_G) grows continuously, reaching a maximum of π in the limit as $\theta \to \pi/2$. As the latitude crosses the equator, the geodesic jumps from one pole to the other pole, resulting in an instantaneous change of sign of this large area and a phase jump of π.

Finally, our approach for testing the geodesic rule is unique for the following reasons: (1) the use of a spatial interference pattern to determine the phase in a single experimental run (no need to scan any parameter to obtain the phase); (2) the use of a common phase reference for both hemispheres while scanning θ, enabling verification of the π phase jump and the sign change; and (3) obtaining the relative phase by allowing the two coherently-prepared wavepackets to expand in free flight and overlap, in contrast to previous atom interferometry studies that required additional manipulation of θ and $\Delta\phi$ to obtain interference.

6.4 T^3 Stern-Gerlach Interferometer

Here we consider an application of the full-loop SGI wherein we minimize the delay times between successive SG pulses as much as allowed by our electronics. In such an extreme scenario, it is expected that the phase accumulation will scale purely as T^3, thus representing the first pure interferometric measurement of the Kennard phase [19] predicted in 1927 [85, 86] (see also [87–89]). The theory for this experiment was done by the group of Wolfgang Schleich.

In order to describe the phase evolution of an atom moving in a time- and state-dependent linear potential, it is sufficient [90] to know the two time-dependent

forces $\mathbf{F}_u \equiv F_u(t)\mathbf{e}_z$ and $\mathbf{F}_l \equiv F_l(t)\mathbf{e}_z$ acting on the atom along the upper and lower branches, respectively, of the interferometer shown in Fig. 8, where z is the axis of gravity, the axis of our longitudinal interferometer, and also the axis of our magnetic gradients.

In the present case, these forces comprise the gravitational force $F_g = mg$ and the state-dependent magnetic forces $\mathbf{F}_i = -\mu_B(g_F)_i(m_F)_i(\partial|\mathbf{B}|/\partial z)\mathbf{e}_z$, $(i = 1, 2)$:

$$F_{u,l}(t) = F_g + F_{2,1}\mathcal{F}(t), \tag{9}$$

where μ_B, g_F, and m_F are the Bohr magneton, the Landé factor, and the projection of the angular momentum on the quantization (y-)axis, respectively. The function $\mathcal{F}(t)$ provides the time-dependent modulation shown as the orange curve in Fig. 8(b):

$$\begin{aligned}\mathcal{F}(t) \equiv &\Theta(t) - \Theta(t - T_1) - \Theta(t - T_1 - T_d) + \Theta(t - 3T_1 - T_d) \\ &+ \Theta(t - 3T_1 - 2T_d) - \Theta(t - 4T_1 - 2T_d).\end{aligned} \tag{10}$$

Here we are using the Heaviside step function $\Theta(t)$ and we are assuming that the duration of each gradient pulse is identical, i.e., $T_{2,3,4} = T_1$, as are the two delay times, $T_{d_1,d_2} = T_d$. We are also careful to ensure experimentally that the magnetic field is linear in the vicinity of the atoms and acts only along the vertical (z-)axis.[3]

As in the full-loop SGI experiments of Sect. 5, we measure the spin population in state $|1\rangle$ which, in this configuration, is a periodic function of the interferometer phase [91].

$$P_1 = \frac{1}{2}\left[1 - \cos\left(\delta\Phi + \varphi_0\right)\right], \tag{11}$$

where

$$\delta\Phi = \frac{1}{\hbar}\int_0^T dt\, \bar{F}(t)\delta z(t), \tag{12}$$

with the total time $T \equiv 4T_1 + 2T_d$. Note that the interferometer will be closed in both position and momentum provided that the differences

$$\delta p(t) = \int_0^t d\tau\, \delta F(\tau) \tag{13}$$

---

[3]Magnetic field linearity is ensured to a good approximation by the three-wire chip design and by carefully positioning the atoms very close to the center of the quadrupole field that they produce, as well as by the short distances that the atomic wavepackets travel ($\sim 1\,\mu$m) compared to their distance from the chip ($\sim 100\,\mu$m). We also adjust the duration of T_4 slightly, relative to T_1, to better optimize the visibility and account for any residual non-linearity. See [19, 68] for further details.
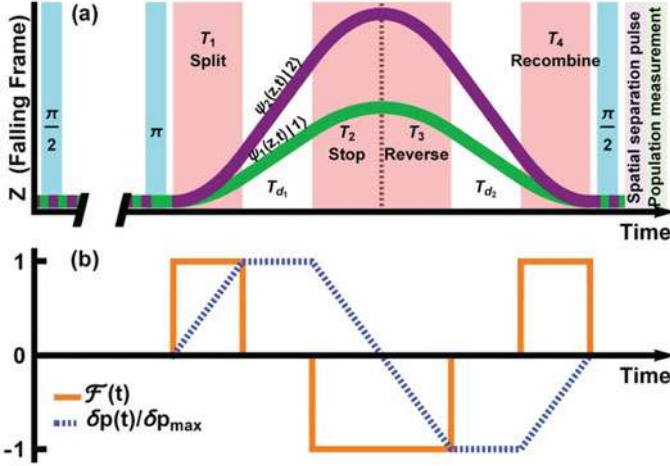
Fig. 8 Pulse sequence of our longitudinal T^3-SGI (not to scale). **a** Trajectories of the atomic wavepackets with internal states $|1\rangle$ (green curve) and $|2\rangle$ (purple curve). Here we are using the freely-falling reference frame (gravity upwards), distinct from the center-of-mass reference frame used for Figs. 2 and 4. Also shown are the RF (blue) and magnetic gradient (red) pulses. The magnetic field gradients result in a state-dependent force along the z-direction while the strong bias magnetic field along the y-direction defines the quantization axis and ensures a two-level system. **b** Time dependence of the relative force $\mathcal{F} = \mathcal{F}(t)$ [orange curve, Eq. (10)] and the corresponding relative momentum $\delta p(t)$ [blue dashed curve, Eq. (13)] between the wavepackets moving along the two interferometer paths. In the experiment, we achieved the maximal separation $\Delta z_{\max} = 1.2\,\mu$m in position and $\Delta p_{\max}/m_{\mathrm{Rb}} = 17$ mm/s in velocity. Reprinted from [19] with permission © (2019) by the American Physical Society

and

$$\delta z(t) = \frac{1}{m} \int\limits_0^t d\tau\, \delta F(\tau)(t - \tau) \tag{14}$$

both vanish at $t = T$. Here φ_0 is a constant phase taking into account possible technical misalignment, while $\bar{F}(t) \equiv [F_u(t) + F_l(t)]/2 = F_g + \frac{1}{2}(F_1 + F_2)\mathcal{F}(t)$ and $\delta F(t) \equiv F_u(t) - F_l(t) = (F_2 - F_1)\mathcal{F}(t)$ are the mean and relative forces respectively. From Eq. (11) we finally obtain

$$\delta\Phi = \frac{mga_B}{\hbar}\left(\frac{\mu_1 - \mu_2}{\mu_B}\right)\left(2T_1^3 + 3T_1^2 T_d + T_1 T_d^2\right)$$
$$+ \frac{ma_B^2}{\hbar}\left(\frac{\mu_1^2 - \mu_2^2}{\mu_B^2}\right)\left(\frac{2}{3}T_1^3 + T_1^2 T_d\right), \tag{15}$$

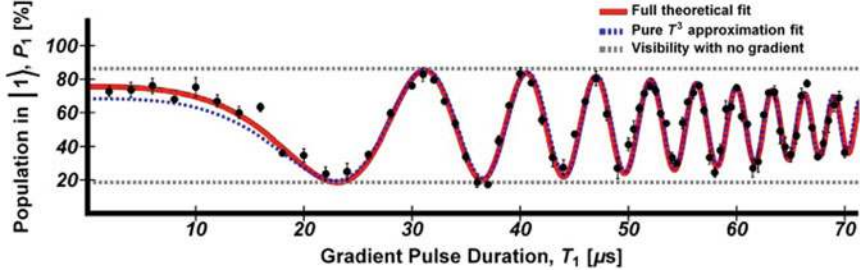with $a_B \equiv \mu_B \nabla B/m$ being the magnetic acceleration.

Fig. 9 Measurement of the cubic phase with the T^3-SGI presented in Fig. 8. The solid red line represents a fit based on Eq. (15), as described in the text. The dashed blue line is a fit with $T_d = 0$, showing that the interferometer phase scales purely as T_1^3 for $T_1 \gtrsim 20\,\mu s$. The visibility drops from 68% to 32% over 70 μs with a decay time of 75 μs. This reduction results from inaccuracies in recombining the two interferometer paths. The dashed gray horizontal lines depict the maximal and minimal values of the population P_1 measured independently without magnetic field gradients. Reprinted from [19] with permission © (2019) by the American Physical Society

As sketched in Fig. 8, the experiment begins with an on-resonance RF $\pi/2$-pulse that transfers the initially prepared internal atomic state $|2\rangle$ to an equal superposition, $\frac{1}{\sqrt{2}}(|1\rangle + |2\rangle)$. This $\pi/2$ pulse is applied 1 ms after the atoms are released from the trap in which they were prepared, in order to ensure that the trapping fields are fully quenched. Following a free-fall time of 400 μs (the first "dark time"), we apply an RF π-pulse that flips the atomic state to $\frac{1}{\sqrt{2}}(|1\rangle - |2\rangle)$. After a second dark time of another 400 μs, a second $\pi/2$ pulse completes the spin-echo sequence. The π-pulse inverts the population between the two states of the system thereby allowing any time-independent phase shift accumulated during the first dark time to be canceled in the second dark time. The experiment is completed by applying a magnetic gradient to separate the spin populations and a subsequent pulse of the detection laser to image both states simultaneously.

As with all our previous full-loop experiments, the four magnetic field gradient pulses are produced by current-carrying wires on the atom chip. This magnetic pulse sequence sends the spin states $|1\rangle$ and $|2\rangle$ along different trajectories in the SGI and ultimately closes the interferometer in both momentum and position. Careful calibration measurements verified that reversing the wire currents (the current flow is reversed during T_2 and T_3 relative to T_1 and T_4) provides magnetic accelerations that are equal in magnitude (but opposite in sign) to within our experimental uncertainty of $< 1\%$.

The experimental data shown in Fig. 9 are measured as a function of the time $2 < T_1 < 70\,\mu s$. From Eq. (15), it is apparent that the T^3 dependence will be most evident if $T_d \ll T_1$, which is satisfied for most of the experimental range by using a fixed experimental value of $T_d = 2.6\,\mu s$ (limited by the speed of our electronic circuits). Note that $T_1 \lesssim 100\,\mu s$ is limited by the duration of the second dark time.

The experimental data (dots) agree very well with the theory (solid red line) based on Eq. (15), where the fitting parameters are the magnetic acceleration a_B as well

as the decay constant of the visibility and a constant phase φ_0. The dashed blue line is obtained by setting $T_d = 0$, leading to a pure T_1^3 scaling that is indistinguishable from the full theoretical fit for $T_1 \gtrsim 20\,\mu s$:

$$\delta\Phi^{(T^3)} \cong \frac{ma_B}{32\hbar} \left(\frac{\mu_1 - \mu_2}{\mu_B} \right) \left(g + \frac{\mu_1 + \mu_2}{3\mu_B}\, a_B \right) T^3. \tag{16}$$

The maximum visibility displayed by the gray lines is first measured by performing only the RF spin-echo sequence ($\pi/2 - \pi - \pi/2$) without the magnetic field gradients and changing the phase of the second $\pi/2$ pulse. The maximal visibility is limited by imperfections in the RF pulses. As discussed above, utilizing an echo sequence allows us to cancel out contributions to the interferometer phase from the bias magnetic field, and to increase the coherence time.

The excellent fit to these data allows a precise determination of the magnetic field acceleration, $a_B^{\text{fit}} = 246.97 \pm 0.09\,\text{m/s}^2$. Separate measurements were used to independently determine the magnetic field gradient using time-of-flight (TOF) techniques, which gave a value of $a_B^{\text{TOF}} = 249 \pm 2\,\text{m/s}^2$.[4] While these measurements agree with one another, the difference in measurement errors clearly shows that our T^3-SGI provides a much more precise measurement of the magnetic field gradient.

Let us now consider the case when $T_1 \ll T_d$, such that during T_d the relative momentum $\delta p_0 \equiv ma_B T_1 (\mu_1 - \mu_2)/\mu_B$ between the paths is kept constant, i.e., we take the magnetic field gradient pulses to be delta functions.

In this limit the interferometer phase from Eq. (15) becomes

$$\delta\Phi^{(T^2)} \cong \frac{\delta p_0}{4\hbar}\, g T^2, \tag{17}$$

scaling quadratically with the total time $T \cong 2T_d$, since we now maintain a piecewise constant momentum difference between the two arms. This is similar to the T^2-SGI [18] or the Kasevich-Chu interferometer [90], although the momentum transfer δp_0 is provided by the magnetic field gradient in the case of the T^2-SGI, rather than by the laser light pulse.

We conclude our discussion of this unique T^3 interferometer by comparing the scaling of the interferometer phases $\delta\Phi^{(T^3)}$ and $\delta\Phi^{(T^2)}$ with the total interferometer time T, as given by Eqs. (16) and (17) respectively. The data in Fig. 10 are taken from Fig. 9 and from our T^2-SGI (when experimentally realizing the condition $T_1 \ll T_d$), showing clearly that the T^3-SGI significantly outperforms the T^2-SGI with respect to total phase accumulation, even though the latter can currently operate for total times T up to three times longer than the former. Finally, let us briefly note that this T^3 realization has already been coined a proof-of-principle experiment for testing the quantum nature of gravity [49].

---

[4]These values for a_B^{fit} and a_B^{TOF} are different from those presented in [19] due to a different fitting procedure used there. A full analysis and fitting procedures are presented in the Appendices of [68].
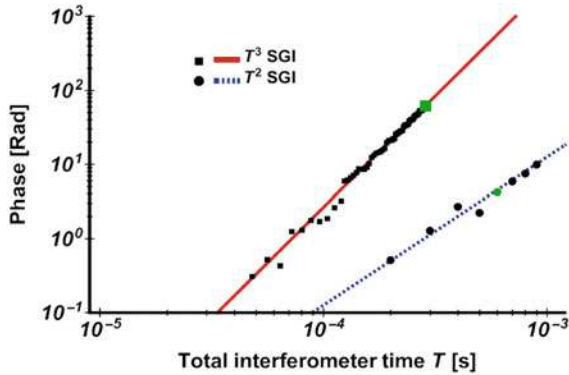
Fig. 10 Scaling of the interferometer phases $\delta\Phi^{(T^3)}$ [squares, Eq.(16)] and $\delta\Phi^{(T^2)}$ [circles, Eq. (17)], as functions of the total interferometer time T. The solid red line is fitted to our data for the T^3-SGI and the dashed blue line is fitted to our T^2-SGI data when experimentally realizing the condition $T_1 \ll T_d$. In its current configuration with $T_{\max} = 285\,\mu$s, the phase of the T^3-SGI is almost six times larger than the phase of the best T^2-SGI, even though the magnetic field gradients and the maximal time $T_{\max} = 924\,\mu$s are larger than those of the T^3-SGI by factors of 2.3 and 3.2, respectively. For reference, the green square and green dot represent data for which the observed visibility is $\approx 30\%$ for both the T^3-SGI and T^2-SGI respectively. Adapted from [19] with permission © (2019) by the American Physical Society

Looking into the future, we may ask if one may extend the T^3 scaling to yet higher powers of time. In the Ramsey-Bordé interferometer [92], the phase shift that scales linearly with the interferometer time T originates from a constant position difference between two paths during most of this time. In the Kasevich-Chu interferometer [93, 94], the quadratic scaling of the phase with time is caused by a piecewise constant velocity difference, while a piecewise constant acceleration difference between the two paths results in the cubic phase scaling $\delta\Phi \propto T^3$, as presented above.

One can generalize this idea to achieve any arbitrary phase scaling by having a piecewise difference in the nth derivative of the position difference between the two paths. By designing an interferometer sequence consisting of pulses with a higher-order time-dependence of the forces, combined with careful choices of the relative signs and durations of the pulses, the total phase can be made to scale with the interferometer time as T^{n+1} for any chosen $n > 2$.

7   Outlook

7.1   SGI with Single Ions

The discovery of the Stern-Gerlach effect led to lively discussions early in the quantum era regarding the possibility of measuring an analogous effect for the electron

itself (see e.g., [95, 96]). The Lorentz force adds the complicating factor of a purely classical deflection of the electron beam that would smear out any expected SG splitting. Here we summarize a generalized semiclassical discussion for any charged particle of mass m and charge e from [62] (though with the co-ordinate system in Table 14.1). Assuming a beam momentum p_x and a transverse beam spatial width Δz, we calculate the spread of the Lorentz force ΔF_L due to a transverse magnetic gradient B' as

$$\Delta F_L = \frac{e}{m} \, p_x B' \Delta z. \tag{18}$$

Since the beam would be well collimated, $\Delta p_z < p_x$, so

$$\Delta F_L > \frac{e}{m} \, B' \Delta p_z \Delta z \geq \frac{e\hbar}{2m} \, B' = \frac{m_e}{m} \times \left(\frac{e\hbar}{2m_e} \, B' \right) = \frac{m_e}{m} \, F_{SG}, \tag{19}$$

where the second inequality uses the uncertainty principle and we have introduced the electron mass m_e to relate F_L to the Stern-Gerlach force F_{SG}.

The spatially inhomogeneous Lorentz broadening is therefore larger than the SG splitting for electrons ($m = m_e$), at least in this semiclassical analysis [97], and this lively controversy has continued for decades though, as far as we know, without any conclusive experimental tests for electrons or for any other charged particles (see [98–100] for reviews of the early history of this issue and recent perspectives). In contrast, Eq. (19) shows no such fundamental problem if we take ions such that $m_e/m < 10^{-3}$, thereby motivating our proposals, including chip-based designs, for measurements using very high-resolution single ion-on-demand sources that have recently been developed using ultra-cold ion traps [61, 101]. As a practical matter, we note that a suitable ion chip could be fabricated and implemented either based on an array of current-carrying wires as analyzed in [62] or on a magnetized microstructure like those implemented in [102, 103].

Although we did not extend our analysis to include the coherence of the spin-dependent splitting, the suggested ion-SG beam splitter may form a basic building block of free-space interferometric devices for charged particles. Here we quote from our collaborative work with Henkel et al. [62]. In addition to measuring the coherence of spin splitting as in the "Humpty-Dumpty" effect (see Sect. 1), we anticipate that such a device could provide new insights concerning the fundamental question of whether and where in the SG device a spin measurement takes place. The ion interference would also be sensitive to Aharonov-Bohm phase shifts arising from the electromagnetic gauge field. The ion source would be a truly single-particle device [61] and eliminate certain problems arising from particle interactions in high-density sources of neutral bosons [104].

Such single-ion SG devices would open the door for a wide spectrum of fundamental experiments, probing for example weak measurements and Bohmian trajectories. The strong electric interactions may also be used, for example, to entangle the single ion with a solid-state quantum device (an electron in a quantum dot or on a Coulomb island, or a qubit flux gate). This type of interferometer may lead to new sensing

capabilities [105]: one of the two ion wavepackets is expected to pass tens to hundreds of nanometers above a surface (in the chip configuration of our proposal [62]) and may probe van der Waals and Casimir-Polder forces, as well as patch potentials. The latter are very important as they are believed to give rise to the anomalous heating observed in miniaturized ion traps [106]. Due to the short distances between the ions and the surface, the device may also be able to sense the gravitational force on small scales [107]. Finally, such a single-ion interferometer may enable searches for exotic physics. These include spontaneous collapse models, the fifth force from a nearby surface, the self-charge interaction between the two ion wavepackets, and so on. Eventually, one may be able to realize a double SG-splitter with different orientations, as originally attempted by Stern, Segrè and co-workers [108, 109], in order to test ideas like the Bohm-Bub non-local hidden variable theory [110–112], or ideas on deterministic quantum mechanics (see, e.g., [113]). Since ions may form the basis of extremely accurate clocks, an ion-SG device would enable clock interferometry at a level sensitive to the Earth's gravitational red-shift (see the proof-of-principle experiments with neutral atoms in [20, 21]). This has important implications for studying the interface between quantum mechanics and general relativity.

7.2 SGI with Massive Objects

The main focus of our future efforts will be to realize an SGI with massive objects. The idea of using the SG interferometer, with a macroscopic object as a probe for gravity, has been detailed in several studies [46, 47, 114, 115] describing a wide range of experiments from the detection of gravitational waves to tests of the quantum nature of gravity. Here we envision using a macroscopic body in the full-loop SGI. We anticipate utilizing spin population oscillations as our interference observable rather than spatial fringes, i.e., density modulations. This observable, as demonstrated in the atomic SGI described above, is advantageous because there is no requirement for long evolution times in order to allow the spatial fringes to develop, nor is high-resolution imaging needed to resolve the spatial fringes. Let us note that there are other proposals to realize a spatial superposition of macroscopic objects [70, 116].

As a specific example, let us consider a solid object comprising $10^6 - 10^{10}$ atoms with a single spin embedded in the solid lattice, e.g., a nano-diamond with a single NV center. Let us first emphasize that even prior to any probing of gravity, a successful SGI will already achieve at least 3 orders of magnitude more atoms than the state-of-the-art in macroscopic-object interferometry [60], thus contributing novel insight to the foundations of quantum mechanics. Another contribution to the foundations of quantum mechanics would be the ability to test continuous spontaneous localization (CSL) models (e.g., [117] and references therein).

When probing gravity, the first contribution of such a massive-object SGI would simply be to measure little g. As the phase is accumulated linearly with the mass, a massive-object interferometer is expected to have much more sensitivity to g than atomic interferometers being used currently (assuming of course that all other fea-

tures are comparable). This is also a method to verify that a massive-object superposition can be created [114, 118, 119]. A second contribution would measure gravity at short distances, since the massive object may be brought close to a surface while in one of the SGI paths, thus enabling probes of the fifth force. Once the SG technology allows the use of large masses, a third contribution will be the testing of hypotheses concerning gravity self-interaction [48, 116], and once large-area interferometry is also enabled, a fourth contribution would be to detect gravitational waves [46]. Finally, placing two such SGIs in parallel next to each other will enable probes of the quantum nature of gravity [47, 120]. Let us emphasize that, although high accelerations may be obtained with multiple spins, we intend to focus on the case of a macroscopic object with a single spin, since the observable of such a quantum-gravity experiment is entanglement, and averaging over many spins may wash out the signal.

To avoid the hindering consequences of the HD effect, one must ensure that the experimental accuracy of the recombination, as discussed in Sect. 5, will be better than the coherence length. Obviously it is very hard to achieve a large coherence length for a massive object, but recent experimental numbers and estimates seem to indicate that this is feasible. Another crucial problem is the coherence time. A massive object has a huge cross section for interacting with the environment (e.g., background gas), but the extremely short interferometer times, as discussed in this review, seem to serve as a protective shield suppressing decoherence. We are currently a detailed account of these considerations [121].

Disclosure Statement The authors declare that they have no competing financial interests.

References

1. W. Gerlach, O. Stern, Der experimentelle Nachweis der Richtungsquantelung im Magnetfeld. Z. Physik **9**, 349 (1922). https://doi.org/10.1007/BF01326983
2. B. Friedrich, D. Herschbach, H. Schmidt-Böcking, J.P. Toennies, An international symposium (Wilhelm and Else Heraeus Seminar #702) marked the centennial of Otto Stern's first molecular beam experiment and the thriving of atomic physics; a European Physical Society Historic Site Was Inaugurated. Front. Phys. **7**, 208 (2019). https://doi.org/10.3389/fphy.2019.00208
3. B. Friedrich, H. Schmidt-Böcking. Otto Stern's molecular beam method and its impact on quantum physics (2020)
4. D. Herschbach, Molecular beams entwined with quantum theory: a bouquet for Max Planck. Ann. Phys. (Leipzig) **10**, 163 (2001). https://doi.org/10.1002/1521-3889(200102)10:1/2<163::AID-ANDP163>3.0.CO;2-W

5. B. Friedrich, D. Herschbach, Stern and Gerlach: how a bad cigar helped reorient atomic physics. Phys. Today **56**, 53 (2003). https://doi.org/10.1063/1.1650229

6. M. Keil, O. Amit, S. Zhou, D. Groswasser, Y. Japha, R. Folman, Fifteen years of cold matter on the atom chip: promise, realizations, and prospects. J. Mod. Opt. **63**, 1840 (2016). https://doi.org/10.1080/09500340.2016.1178820

7. J. Reichel, W. Hänsel, T.W. Hänsch, Atomic micromanipulation with magnetic surface traps. Phys. Rev. Lett. **83**, 3398 (1999). https://doi.org/10.1103/PhysRevLett.83.3398

8. R. Folman, P. Krüger, D. Cassettari, B. Hessmo, T. Maier, J. Schmiedmayer, Controlling cold atoms using nanofabricated surfaces: atom chips. Phys. Rev. Lett. **84**, 4749 (2000). https://doi.org/10.1103/PhysRevLett.84.4749

9. N.H. Dekker, C.S. Lee, V. Lorent, J.H. Thywissen, S.P. Smith, M. Drndić, R.M. Westervelt, M. Prentiss, Guiding neutral atoms on a chip. Phys. Rev. Lett. **84**, 1124 (2000). https://doi.org/10.1103/PhysRevLett.84.1124

10. R. Folman, P. Krüger, J. Schmiedmayer, J. Denschlag, C. Henkel, Microscopic atom optics: from wires to an atom chip. Adv. At. Mol. Opt. Phys. **48**, 263 (2002). https://doi.org/10.1016/S1049-250X(02)80011-8

11. J. Reichel, Microchip traps and Bose-Einstein condensation. Appl. Phys. B **74**, 469 (2002). https://doi.org/10.1007/s003400200861

12. J. Fortágh, C. Zimmermann, Magnetic microtraps for ultracold atoms. Rev. Mod. Phys. **79**, 235 (2007). https://doi.org/10.1103/RevModPhys.79.235

13. *Atom Chips,* J. Reichel, V. Vuletić, eds. (Wiley-VCH, Hoboken, NJ, 2011). https://doi.org/10.1002/9783527633357

14. R. Folman, Material science for quantum computing with atom chips, in *Special Issue on Neutral Particles,*, ed. by R. Folman. Quantum Inf. Process. **10**, 995 (2011), https://doi.org/10.1007/s11128-011-0311-5

15. https://in.bgu.ac.il/en/nano-fab

16. S. Machluf, Y. Japha, R. Folman, Coherent Stern-Gerlach momentum splitting on an atom chip. Nature Commun. **4**, 2424 (2013). https://doi.org/10.1038/ncomms3424

17. Y. Margalit, Z. Zhou, S. Machluf, Y. Japha, S. Moukouri, R. Folman, Analysis of a high-stability Stern-Gerlach spatial fringe interferometer. New J. Phys. **21**, 073040 (2019). https://doi.org/10.1088/1367-2630/ab2fdc

18. Y. Margalit, Z. Zhou, O. Dobkowski, Y. Japha, D. Rohrlich, S. Moukouri, R. Folman, Realization of a complete Stern-Gerlach interferometer. arXiv:1801.02708v2 (2018)

19. O. Amit, Y. Margalit, O. Dobkowski, Z. Zhou, Y. Japha, M. Zimmermann, M.A. Efremov, F.A. Narducci, E.M. Rasel, W.P. Schleich, R. Folman, T^3 Stern-Gerlach matter-wave interferometer. Phys. Rev. Lett. **123**, 083601 (2019). https://doi.org/10.1103/PhysRevLett.123.083601

20. Y. Margalit, Z. Zhou, S. Machluf, D. Rohrlich, Y. Japha, R. Folman, A self-interfering clock as a which-path witness. Science **349**, 1205 (2015). https://doi.org/10.1126/science.aac6498

21. Z. Zhou, Y. Margalit, D. Rohrlich, Y. Japha, R. Folman, Quantum complementarity of clocks in the context of general relativity. Class. Quantum Grav. **35**, 185003 (2018). https://doi.org/10.1088/1361-6382/aad56b

22. A.D. Cronin, J. Schmiedmayer, D.E. Pritchard, Optics and interferometry with atoms and molecules. Rev. Mod. Phys. **81**, 1051 (2009). https://doi.org/10.1103/RevModPhys.81.1051

23. W. Heisenberg. *Die Physikalischen Prinzipien der Quantentheorie*. (S. Hirzel: Leipzig 1930); *The Physical Principles of the Quantum Theory* transl. by C. Eckart, F. C. Hoyt (Dover, Mineola, NY, 1950)

24. D. Bohm, *Quantum Theory* (Prentice-Hall, Englewood Cliffs, 1951), pp. 604–605

25. E.P. Wigner, The problem of measurement. Am. J. Phys. **31**, 6 (1963). https://doi.org/10.1119/1.1969254

26. H. J. Briegel, B.-G. Englert, M.O. Scully, H. Walther, Atom interferometry and the quantum theory of measurement, in *Atom Interferometry*, P.R. Berman, ed. (Academic Press, New York, 1997), p. 240

27. This popular version of the English nursery rhyme appears in https://en.wikipedia.org/wiki/Humpty_Dumpty

28. B.-G. Englert, J. Schwinger, M.O. Scully, Is spin coherence like Humpty-Dumpty? I. Simplified treatment. Found. Phys. **18**, 1045 (1988). https://doi.org/10.1007/BF01909939

29. J. Schwinger, M.O. Scully, B.-G. Englert, Is spin coherence like Humpty-Dumpty? II. General theory. Z. Phys. D **10**, 135 (1988). https://doi.org/10.1007/BF01384847

30. M.O. Scully, B.-G. Englert, J. Schwinger, Spin coherence and Humpty-Dumpty. III. The effects of observation. Phys. Rev. A **40**, 1775 (1989). https://doi.org/10.1103/PhysRevA.40.1775

31. B.-G. Englert, Time reversal symmetry and Humpty-Dumpty. Z. Naturforsch A **52**, 13 (1997). https://doi.org/10.1515/zna-1997-1-206

32. M. O. Scully, Jr. W.E. Lamb, A. Barut, On the theory of the Stern-Gerlach apparatus. Found. Phys. **17**, 575 (1987).https://doi.org/10.1007/BF01882788

33. T.R. de Oliveira, A.O. Caldeira, Dissipative Stern-Gerlach recombination experiment. Phys. Rev. A **73**, 042502 (2006). https://doi.org/10.1103/PhysRevA.73.042502

34. M. Devereux, Reduction of the atomic wavefunction in the Stern-Gerlach magnetic field. Can. J. Phys. **93**, 1382 (2015). https://doi.org/10.1139/cjp-2015-0031

35. J. Robert, C. Miniatura, S. Le Boiteux, J. Reinhardt, V. Bocvarski, J. Baudon, Atomic interferometry with metastable hydrogen atoms. Europhys. Lett. **16**, 29 (1991). https://doi.org/10.1209/0295-5075/16/1/006

36. C. Miniatura, F. Perales, G. Vassilev, J. Reinhardt, J. Robert, J. Baudon, A longitudinal Stern-Gerlach interferometer: the "beaded" atom. J. Phys. II **1**, 425 (1991). https://doi.org/10.1051/jp2:1991177

37. C. Miniatura, J. Robert, S. Le Boiteux, J. Reinhardt, J. Baudon, A longitudinal Stern-Gerlach atomic interferometer. App. Phys. B **54**, 347 (1992). https://doi.org/10.1007/BF00325378

38. J. Robert, C. Miniatura, O. Gorceix, S. Le Boiteux, V. Lorent, J. Reinhardt, J. Baudon, Atomic quantum phase studies with a longitudinal Stern-Gerlach interferometer. J. Phys. II **11**, 601 (1992). https://doi.org/10.1051/jp2:1992155

39. C. Miniatura, J. Robert, O. Gorceix, V. Lorent, S. Le Boiteux, J. Reinhardt, J. Baudon, Atomic interferences and the topological phase. Phys. Rev. Lett. **69**, 261 (1992). https://doi.org/10.1103/PhysRevLett.69.261

40. S. Nic Chormaic, V. Wiedemann, C. Miniatura, J. Robert, S. Le Boiteux, V. Lorent, O. Gorceix, S. Feron, J. Reinhardt, J. Baudon, Longitudinal Stern-Gerlach atomic interferometry using velocity selected atomic beams. J. Phys. B **26**, 1271 (1993). https://doi.org/10.1088/0953-4075/26/7/011

41. J. Baudon, R. Mathevet, J. Robert, Atomic interferometry. J. Phys. B **32**, R173 (1999). https://doi.org/10.1088/0953-4075/32/15/201

42. M. Boustimi, V. Bocvarski, K. Brodsky, F. Perales, J. Baudon, J. Robert, Atomic interference patterns in the transverse plane. Phys. Rev. A **61**, 033602 (2000). https://doi.org/10.1103/PhysRevA.61.033602

43. E. Maréchal, R. Long, T. Miossec, J.-L. Bossennec, R. Barbé, J.-C. Keller, O. Gorceix, Atomic spatial coherence monitoring and engineering with magnetic fields. Phys. Rev. A **62**, 53603 (2000). https://doi.org/10.1103/PhysRevA.62.053603

44. B. Viaris de Lesegno, J.C. Karam, M. Boustimi, F. Perales, C. Mainos, J. Reinhardt, J. Baudon, V. Bocvarski, D. Grancharova, F. Pereira Dos Santos, T. Durt, H. Haberland J. Robert, Stern Gerlach interferometry with metastable argon atoms: an immaterial mask modulating the profile of a supersonic beam. Eur. Phys. J. D **23**,25 (2003). https://doi.org/10.1140/epjd/e2003-00023-y

45. K. Rubin, M. Eminyan, F. Perales, R. Mathevet, K. Brodsky, B. Viaris de Lesegno, J. Reinhardt, M. Boustimi, J. Baudon, J.-C. Karam, J. Robert, Atom interferometer using two Stern-Gerlach magnets. Laser Phys. Lett. **1**, 184 (2004). https://doi.org/10.1002/lapl.200310047

46. R.J. Marshman, A. Mazumdar, G.W. Morley, P.F. Barker, S. Hoekstra, S. Bose, Mesoscopic interference for metric and curvature (MIMAC) & gravitational wave detection. New J. Phys. **22**, 083012 (2020). https://doi.org/10.1088/1367-2630/ab9f6c

47. S. Bose, A. Mazumdar, G.W. Morley, H. Ulbricht, M. Toroš, M. Paternostro, A.A. Geraci, P.F. Barker, M.S. Kim, G. Milburn, Spin entanglement witness for quantum gravity. Phys. Rev. Lett. **119**, 240401 (2017). https://doi.org/10.1103/PhysRevLett.119.240401

48. M. Hatifi, T. Durt, Revealing self-gravity in a Stern-Gerlach Humpty-Dumpty experiment. arXiv:2006.07420 (2020)

49. C. Marletto, V. Vedral, On the testability of the equivalence principle as a gauge principle detecting the gravitational t^3 phase. Front. Phys. **8**, 176 (2020). https://doi.org/10.3389/fphy.2020.00176

50. M. Gebbe, S. Abend, J.-N. Siemß, M. Gersemann, H. Ahlers, H.Müntinga, S. Herrmann, N. Gaaloul, C. Schubert, K. Hammerer, C. Lämmerzahl, W. Ertmer, E.M. Rasel, Twin-lattice atom interferometry. arXiv:1907.08416v1 (2019)

51. B. Canuel, S. Abend, P. Amaro-Seoane, F. Badaracco, Q. Beaufils, A. Bertoldi, K. Bongs, P. Bouyer, C. Braxmaier, W. Chaibi, N. Christensen, F. Fitzek, G. Flouris, N. Gaaloul, S. Gaffet, C.L. Garrido Alzar, R. Geiger, S. Guellati-Khelifa, K. Hammerer, J. Harms, J. Hinderer, M. Holynski, J. Junca, S. Katsanevas, C. Klempt, C. Kozanitis, M. Krutzik, A. Landragin, I. Làzaro Roche, B. Leykauf, Y.-H. Lien, S. Loriani, S. Merlet, M. Merzougui, M. Nofrarias, P. Papadakos, F. Pereira dos Santos, A. Peters, D. Plexousakis, M. Prevedelli, E.M. Rasel, Y. Rogister, S. Rosat, A. Roura, D. O. Sabulsky, V. Schkolnik, D. Schlippert, C. Schubert, L. Sidorenkov, J.-N. Siemß, C. F. Sopuerta, F. Sorrentino, C. Struckmann, G.M. Tino, G. Tsagkatakis, A. Viceré, W. von Klitzing, L. Woerner, X. Zou, Technologies for the ELGAR large scale atom interferometer array. arXiv:2007.04014v1 (2020); ELGAR–a European Laboratory for Gravitation and Atom-interferometric Research. Class. Quantum Grav. **37**, 225017 (2020). https://doi.org/10.1088/1361-6382/aba80e

52. J. Rudolph, T. Wilkason, M. Nantel, H. Swan, C.M. Holland, Y. Jiang, B.E. Garber, S.P. Carman, J.M. Hogan, Large momentum transfer clock atom interferometry on the 689 nm intercombination line of strontium. Phys. Rev. Lett. **124**, 083604 (2020). https://doi.org/10.1103/PhysRevLett.124.083604

53. D.V. Strekalov, N. Yu, K. Mansour, *Sub-shot Noise Power Source for Microelectronics*. NASA Tech Briefs (Pasadena, CA, 2011). http://ntrs.nasa.gov/archive/nasa/casi.ntrs.nasa.gov/20120006513.pdf

54. E. Danieli, J. Perlo, B. Blümich, F. Casanova, Highly stable and finely tuned magnetic fields generated by permanent magnet assemblies. Phys. Rev. Lett. **110**, 180801 (2013). https://doi.org/10.1103/PhysRevLett.110.180801

55. S. Zhou, D. Groswasser, M. Keil, Y. Japha, R. Folman, Robust spatial coherence 5 μm from a room-temperature atom chip. Phys. Rev. A **93**, 063615 (2016). https://doi.org/10.1103/PhysRevA.93.063615

56. P. Treutlein, P. Hommelhoff, T. Steinmetz, T.W. Hänsch, J. Reichel, Coherence in microchip traps. Phys. Rev. Lett. **92**, 203005 (2004). https://doi.org/10.1103/PhysRevLett.92.203005

57. F. Cerisola, Y. Margalit, S. Machluf, A.J. Roncaglia, J.P. Paz, R. Folman, Using a quantum work meter to test non-equilibrium fluctuation theorems. Nature Commun. **8**, 1241 (2017). https://doi.org/10.1038/s41467-017-01308-7

58. B.S. Zhao, W. Zhang, W. Schöllkopf, Non-destructive quantum reflection of helium dimers and trimers from a plane ruled grating. Mol. Phys. **111**, 1772 (2013). https://doi.org/10.1080/00268976.2013.787150

59. S. Zeller, M. Kunitski, J. Voigtsberger, A. Kalinin, A. Schottelius, C. Schober, M. Waitz, H. Sann, A. Hartung, T. Bauer, M. Pitzer, F. Trinter, C. Goihl, C. Janke, M. Richter, G. Kastirke, M. Weller, A. Czasch, M. Kitzler, M. Braune, R.E. Grisenti, W. Schöllkopf, L.P.H. Schmidt, M.S. Schöffler, J.B. Williams, T. Jahnke, R.Dörner, Imaging the He$_2$ quantum halo state using a free electron laser. Proc. Natl. Acad. Sci. USA **113**, 14651 (2016). https://doi.org/10.1073/pnas.1610688113

60. Y.Y. Fein, P. Geyer, P. Zwick, F. Kiałka, S. Pedalino, M. Mayor, S. Gerlich, M. Arndt, Quantum superposition of molecules beyond 25 kDa. Nature Phys. **15**, 1242 (2019). https://doi.org/10.1038/s41567-019-0663-9

61. G. Jacob, K. Groot-Berning, S. Wolf, S. Ulm, L. Couturier, S.T. Dawkins, U.G. Poschinger, F. Schmidt-Kaler, K. Singer, Transmission microscopy with nanometer resolution using a deterministic single ion source. Phys. Rev. Lett. **117**, 043001 (2016). https://doi.org/10.1103/PhysRevLett.117.043001

62. C. Henkel, G. Jacob, F. Stopp, F. Schmidt-Kaler, M. Keil, Y. Japha, R. Folman, Stern-Gerlach splitting of low-energy ion beams. New J. Phys. **21**, 083022 (2019). https://doi.org/10.1088/1367-2630/ab36c7

63. L.W. Bruch, W. Schöllkopf, J.P. Toennies, The formation of dimers and trimers in free jet ^{4}He cryogenic expansions. J. Chem. Phys. **117**, 1544 (2002). https://doi.org/10.1063/1.1486442

64. Y. Margalit, *Stern-Gerlach Interferometry with Ultracold Atoms*. (Ph.D. Thesis, Ben-Gurion University, 2018). http://www.bgu.ac.il/atomchip/Theses/Yair_Margalit_PhD_Thesis_2018.pdf

65. F. Kiałka, B.A. Stickler, K. Hornberger, Y.Y. Fein, P. Geyer, L. Mairhofer, S. Gerlich, M. Arndt, Concepts for long-baseline high-mass matter-wave interferometry. Phys. Scripta **94**, 034001 (2019). https://doi.org/10.1088/1402-4896/aaf243

66. D.A. Steck. Rubidium 87 D Line Data (2003). https://steck.us/alkalidata/rubidium87numbers.1.6.pdf

67. S. Machluf, *Coherent Splitting of Matter-Waves on an Atom Chip Using a State-Dependent Magnetic Potential* (Ph.D. Thesis, Ben-Gurion University, 2013). http://www.bgu.ac.il/atomchip/Theses/Shimon_Machluf_PhD_2013.pdf

68. O. Amit, *Matter-Wave Interferometry on an Atom Chip* (Ph.D. Thesis, Ben-Gurion University, 2020). http://www.bgu.ac.il/atomchip/Theses/PhD_Thesis_Omer_Amit_submitted.pdf

69. D.E. Miller, J.R. Anglin, J.R. Abo-Shaeer, K. Xu, J.K. Chin, W. Ketterle, High-contrast interference in a thermal cloud of atoms. Phys. Rev. A **71**, 043615 (2005). https://doi.org/10.1103/PhysRevA.71.043615

70. O. Romero-Isart, Coherent inflation for large quantum superpositions of levitated microspheres. New J. Phys. **19**, 719711 (2017). https://doi.org/10.1088/1367-2630/aa99bf

71. R. Colella, A.W. Overhauser, S.A. Werner, Observation of gravitationally induced quantum interference. Phys. Rev. Lett. **34**, 1472 (1975). https://doi.org/10.1103/PhysRevLett.34.1472

72. M. Zych, F. Costa, I. Pikovski, Č. Brukner, Quantum interferometric visibility as a witness of general relativistic proper time. Nature Commun. **2**, 505 (2011). https://doi.org/10.1038/ncomms1498

73. S. Dimopoulos, P.W. Graham, J.M. Hogan, M.A. Kasevich, Testing general relativity with atom interferometry. Phys. Rev. Lett. **98**, 111102 (2007). https://doi.org/10.1103/PhysRevLett.98.111102

74. H. Müntinga, H. Ahlers, M. Krutzik, A. Wenzlawski, S. Arnold, D. Becker, K. Bongs, H. Dittus, H. Duncker, N. Gaaloul, C. Gherasim, E. Giese, C. Grzeschik, T.W. Hänsch, O. Hellmig, W. Herr, S. Herrmann, E. Kajari, S. Kleinert, C. Lämmerzahl, W. Lewoczko-Adamczyk, J. Malcolm, N. Meyer, R. Nolte, A. Peters, M. Popp, J. Reichel, A. Roura, J. Rudolph, M. Schiemangk, M. Schneider, S.T. Seidel, K. Sengstock, V. Tamma, T. Valenzuela, A. Vogel, R. Walser, T. Wendrich, P. Windpassinger, W. Zeller, T. van Zoest, W. Ertmer, W.P. Schleich, E.M. Rasel, Interferometry with Bose-Einstein condensates in microgravity. Phys. Rev. Lett. **110**, 093602 (2013). https://doi.org/10.1103/PhysRevLett.110.093602

75. C.C.N. Kuhn, G.D. McDonald, K.S. Hardman, S. Bennetts, P.J. Everitt, P.A. Altin, J.E. Debs, J.D. Close, N.P. Robins, A. Bose-condensed, simultaneous dual-species Mach-Zehnder atom interferometer. New J. Phys. **16**, 073035 (2014). https://doi.org/10.1088/1367-2630/16/7/073035

76. I. Pikovski, M. Zych, F. Costa, Č. Brukner, Universal decoherence due to gravitational time dilation. Nat. Phys. **11**, 668 (2015). https://doi.org/10.1038/nphys3366

77. B.-G. Englert, Fringe visibility and which-way information: an inequality. Phys. Rev. Lett. **77**, 2154 (1996). https://doi.org/10.1103/PhysRevLett.77.2154

78. E. Giese, A. Friedrich, F. Di Pumpo, A. Roura, W.P. Schleich, D.M. Greenberger, E.M. Rasel, Proper time in atom interferometers: diffractive versus specular mirrors. Phys. Rev. Lett. **99**, 013627 (2019). https://doi.org/10.1103/PhysRevA.99.013627

79. M. Lugli, *Mass and Proper Time as Conjugated Observables* (Graduate Thesis, Università degli Studi di Pavia, Italy, 2017). http://arxiv.org/abs/1710.06504

80. J. Samuel, R. Bhandari, General setting for Berry's phase. Phys. Rev. Lett. **60**, 2339 (1988). https://doi.org/10.1103/PhysRevLett.60.2339

81. R. Bhandari, SU(2) phase jumps and geometric phases. Phys. Lett. A **157**, 221 (1991). https://doi.org/10.1016/0375-9601(91)90055-D

82. T. van Dijk, H.F. Schouten, T.D. Visser, Geometric interpretation of the Pancharatnam connection and non-cyclic polarization changes. J. Am. Opt. Soc. A **27**, 1972 (2010). https://doi.org/10.1364/JOSAA.27.001972

83. S. Pancharatnam, Generalized theory of interference, and its applications. Proc. Indian Acad. Sci. A **44**, 247 (1956). https://doi.org/10.1007/BF03046050

84. Z. Zhou, Y. Margalit, S. Moukouri, Y. Meir, R. Folman, An experimental test of the geodesic rule proposition for the noncyclic geometric phase. Sci. Adv. **6**, eaay8345 (2020). https://doi.org/10.1126/sciadv.aay8345

85. E.H. Kennard, Zur Quantenmechanik einfacher Bewegungstypen. Z. fur Physik **44**, 326 (1927). https://doi.org/10.1007/BF01391200

86. E.H. Kennard, The quantum mechanics of an electron or other particle. J. Franklin Inst. **207**, 47 (1929). https://doi.org/10.1016/S0016-0032(29)91274-6

87. G.G. Rozenman, M. Zimmermann, M.A. Efremov, W.P. Schleich, L. Shemer, A. Arie, Amplitude and phase of wave packets in a linear potential. Phys. Rev. Lett. **122**, 124302 (2019). https://doi.org/10.1103/PhysRevLett.122.124302

88. G.G. Rozenman, L. Shemer, A. Arie, Observation of accelerating solitary wavepackets. Phys. Rev. E **101**, 050201(R) (2020). https://doi.org/10.1103/PhysRevE.101.050201

89. G.G. Rozenman, M. Zimmermann, M.A. Efremov, W.P. Schleich, W.B. Case, D.M. Greenberger, L. Shemer, A. Arie, Projectile motion of surface gravity water wave packets: An analogy to quantum mechanics. Eur. Phys. J. Spec. Top. (2021). https://doi.org/10.1140/epjs/s11734-021-00096-y

90. M. Zimmermann, M. Efremov, W. Zeller, W. Schleich, J. Davis, F. Narducci, Representation-free description of atom interferometers in time-dependent linear potentials. New J. Phys. **21**, 073031 (2019). https://doi.org/10.1088/1367-2630/ab2e8c

91. M. Efremov, M. Zimmermann, O. Amit, Y. Margalit, R. Folman, W. Schleich, Atomic interferometer sensitive to time-dependent acceleration. In preparation (2021)

92. C.J. Bordé, Atomic interferometry with internal state labelling. Phys. Lett. A **140**, 10 (1989). https://doi.org/10.1016/0375-9601(89)90537-9

93. M. Kasevich, S. Chu, Atomic interferometry using stimulated Raman transitions. Phys. Rev. Lett. **67**, 181 (1991). https://doi.org/10.1103/PhysRevLett.67.181

94. A. Peters, K. Chung, S. Chu, High-precision gravity measurements using atom interferometry. Metrologia **38**, 25 (2001). https://doi.org/10.1088/0026-1394/38/1/4

95. L. Brillouin, Is it possible to test by a direct experiment the hypothesis of the spinning electron? Proc. Natl. Acad. Sci. **14**, 755 (1928). https://doi.org/10.1073/pnas.14.10.755

96. N. Bohr, Chemistry and the quantum theory of atomic constitution. J. Chem. Soc. **349**, (1932). https://doi.org/10.1039/JR9320000349

97. G.A. Gallup, H. Batelaan, T.J. Gay, Quantum-mechanical analysis of a longitudinal Stern-Gerlach effect. Phys. Rev. Lett. **86**, 4508 (2001). https://doi.org/10.1103/PhysRevLett.86.4508

98. H. Batelaan, T.J. Gay, J.J. Schwendiman, Stern-Gerlach effect for electron beams. Phys. Rev. Lett. **79**, 4517 (1997). https://doi.org/10.1103/PhysRevLett.79.4517

99. H. Batelaan, Electrons, Stern-Gerlach magnets, and quantum mechanical propagation. Am. J. Phys. **70**, 325 (2002). https://doi.org/10.1119/1.1450559

100. B.M. Garraway, S. Stenholm, Does a flying electron spin? Contemp. Phys. **43**, 147 (2002). https://doi.org/10.1080/00107510110102119

101. G. Jacob, *Ion Implantation and Transmission Microscopy with Nanometer Resolution Using a Deterministic Ion Source*. (Ph.D. Dissertation, Johannes-Gutenberg-Universität, Mainz, Germany, 2016). https://www.quantenbit.physik.uni-mainz.de/files/2019/10/DissSW.pdf

102. E.A. Hinds, I.G. Hughes, Magnetic atom optics: Mirrors, guides, traps, and chips for atoms. J. Phys. D **32**, R119–R146 (1999). http://iopscience.iop.org/article/10.1088/0022-3727/32/18/201/pdf

103. T.D. Tran, Y. Wang, A. Glaetzle, S. Whitlock, A. Sidorov, P. Hannaford, Magnetic lattices for ultracold atoms (2019). arXiv:1906.08918

104. G.M. Tino, M.A. Kasevich, eds., Atom iterferometry, in *Proceedings of International School of Physics "Enrico Fermi"*. http://ebooks.iospress.nl/volume/atom-interferometry, Vol 188 (IOS Press, Amsterdam, 2014)

105. F. Hasselbach, Progress in electron- and ion-interferometry. Rep. Prog. Phys. **73**, 016101 (2010). https://doi.org/10.1088/0034-4885/73/1/016101

106. M. Brownnutt, M. Kumph, P. Rabl, R. Blatt, Ion-trap measurements of electric-field noise near surfaces. Rev. Mod. Phys. **87**, 1419 (2015). https://doi.org/10.1103/RevModPhys.87.1419

107. R.O. Behunin, D.A.R. Dalvit, R.S. Decca, C.C. Speake, Limits on the accuracy of force sensing at short separations due to patch potentials. Phys. Rev. D **89**, 051301(R) (2014). https://doi.org/10.1103/PhysRevD.89.051301

108. T.E. Phipps, O. Stern, Über die Einstellung der Richtungsquantelung. Z. Phys. **73**, 185 (1932). https://doi.org/10.1007/BF01351212

109. R. Frisch, E. Segrè, Über die Einstellung der Richtungsquantelung II. Z. Phys. **80**, 610 (1933). https://doi.org/10.1007/BF01335699

110. D. Bohm, J. Bub, A proposed solution of the measurement problem in quantum mechanics by a hidden variable theory. Rev. Mod. Phys. **38**, 453 (1966). https://doi.org/10.1103/RevModPhys.38.453

111. R. Folman, A search for hidden variables in the domain of high energy physics. Found. Phys. Lett. **7**, 191 (1994). https://doi.org/10.1007/BF02415510

112. S. Das, M. Nöth, D. Dürr, Exotic Bohmian arrival times of spin-1/2 particles: an analytical treatment. Phys. Rev. A **99**, 052124 (2019). https://doi.org/10.1103/PhysRevA.99.052124

113. L.S. Schulman, Program for the special state theory of quantum measurement. Entropy **19**, 343 (2017). https://doi.org/10.3390/e19070343

114. C. Wan, M. Scala, G.W. Morley, A.A.T.M. Rahman, H. Ulbricht, J. Bateman, P.F. Barker, S. Bose, M.S. Kim, Free nano-object Ramsey interferometry for large quantum superpositions. Phys. Rev. Lett. **117**, 143003 (2016). https://doi.org/10.1103/PhysRevLett.117.143003

115. R.J. Marshman, A. Mazumdar, S. Bose, Locality and entanglement in table-top testing of the quantum nature of linearized gravity. Phys. Rev. A **101**, 052110 (2020). https://doi.org/10.1103/PhysRevA.101.052110

116. H. Pino, J. Prat-Camps, K. Sinha, B.P. Venkatesh, O. Romero-Isart, On-chip quantum interference of a superconducting microsphere. Quantum Sci. Technol. **3**, 25001 (2018). https://doi.org/10.1088/2058-9565/aa9d15

117. O. Romero-Isart, Quantum superposition of massive objects and collapse models. Phys. Rev. A **84**, 052121 (2011). https://doi.org/10.1103/PhysRevA.84.052121

118. M. Scala, M.S. Kim, G.W. Morley, P.F. Barker, S. Bose, Matter-wave interferometry of a levitated thermal nano-oscillator induced and probed by a spin. Phys. Rev. Lett. **111**, 180403 (2013). https://doi.org/10.1103/PhysRevLett.111.180403

119. M. Toroš, S. Bose, P.F. Barker, Atom-Nanoparticle Schrödinger Cats. arXiv:2005.12006 (2020)

120. C. Marletto, V. Vedral, Gravitationally induced entanglement between two massive particles is sufficient evidence of quantum effects in gravity. Phys. Rev. Lett. **119**, 240402 (2017). https://doi.org/10.1103/PhysRevLett.119.240402

121. Y. Margalit, O. Dobkowski, Z. Zhou, O. Amit, Y. Japha, S. Moukouri, D. Rohrlich, A. Mazumdar, S. Bose, C. Henkel, R. Folman, Realization of a complete Stern-Gerlach interferometer: towards a test of quantum gravity (2020). https://arxiv.org/pdf/2011.10928v1.pdf